

Unconventional domain tessellations in moiré-of-moiré lattices

<https://doi.org/10.1038/s41586-025-08932-0>

Received: 16 February 2024

Accepted: 24 March 2025

Published online: 14 May 2025

 Check for updates

Daesung Park^{1,2,11}, Changwon Park^{3,4,11}, Kunihiro Yananose^{3,11}, Eunjung Ko³, Byunghyun Kim¹, Rebecca Engelke⁵, Xi Zhang⁶, Konstantin Davydov⁶, Matthew Green⁶, Hyun-Mi Kim⁷, Sang Hwa Park², Jae Heon Lee², Seul-Gi Kim⁷, Hyeongkeun Kim⁷, Kenji Watanabe⁸, Takashi Taniguchi⁹, Sang Mo Yang², Ke Wang⁶, Philip Kim⁵, Young-Woo Son³✉ & Hyobin Yoo^{1,2,10}✉

Imposing incommensurable periodicity on the periodic atomic lattice can lead to complex structural phases consisting of locally periodic structure bounded by topological defects^{1–8}. Twisted trilayer graphene (TTG) is an ideal material platform to study the interplay between different atomic periodicities, which can be tuned by twist angles between the layers, leading to moiré-of-moiré lattices^{9–26}. Interlayer and intralayer interactions between two interfaces in TTG transform this moiré-of-moiré lattice into an intricate network of domain structures at small twist angles, which can harbour exotic electronic behaviours^{9–26}. Here we report a complete structural phase diagram of TTG with atomic-scale lattice reconstruction. Using transmission electron microscopy (TEM) combined with a new interatomic potential simulation^{27,28}, we show several large-scale moiré lattices, including triangular, kagome and a corner-shared hexagram-shaped domain pattern. Each domain is bounded by a 2D network of domain-wall lattices. In the limit of small twist angles, two competing structural orders—rhombohedral and Bernal stackings—with a slight energy difference cause unconventional lattice reconstruction with spontaneous symmetry breaking (SSB) and nematic instability, highlighting the importance of long-range interlayer interactions across entire van der Waals layers. The diverse tessellation of distinct domains, whose topological network can be tuned by the adjustment of the twist angles, establishes TTG as a platform for exploring the interplay between emerging quantum properties and controllable nontrivial lattices.

Interfaces formed by joining two van der Waals crystals has offered a new route to engineer interfacial electronic states by moiré superlattice^{7,29–33}. At low twist angles, the atomic-scale lattice reconstruction becomes appreciable within a superlattice domain, affecting the quasiperiodic electronic structures in the moiré superlattice. In twisted bilayer graphene (TBG), this lattice reconstruction effect can realize anomalous electronic transport and the strongly correlated behaviour^{7,29–32}. As the number of quasiperiodic interfaces increases in multilayer twisted systems, extensive lattice reconstruction leads to the interplay between moiré superlattices formed within individual interfaces. Revealing the resulting hierarchical quasiperiodic structures modulated by the lattice reconstruction is essential for explaining the unusual electronic structures recently reported in multilayer twisted graphene^{9–26,34}.

TTG provides a simplified platform on which the hierarchical structures are evident. The interference pattern between two moiré lattices, such as those between the bottom and middle layers and between

the middle and top layers, generates moiré-of-moiré lattices governing electronic properties^{9–26}. If the reconstruction strength is insufficient, the hierarchical structure remains incommensurate, exhibiting quasicrystal physics^{21,22}. Recent studies^{9–26} on various pairs of twist angles in TTG indicate that the lattice reconstruction modulates the quasiperiodic moiré-of-moiré lattices. However, these studies have focused on twist angles typically exceeding 1.0°, at which the reconstruction strength is insufficient to reveal the unique reconstruction characteristics in TTG.

We emphasize that TTG presents Bernal and rhombohedral stacking orders competing with slight but critical energy difference^{35–38}, unlike TBG. Owing to the presence of two disparate low-energy stackings in TTG, the lattice reconstruction pattern can exhibit qualitatively different structural orderings on tuning the reconstruction strength, providing a new pathway to engineer domain structures. This effect becomes more pronounced with the stronger lattice reconstruction, given the minute energy difference between Bernal and rhombohedral

¹Department of Materials Science and Engineering, Seoul National University, Seoul, Republic of Korea. ²Department of Physics, Sogang University, Seoul, Republic of Korea. ³Korea Institute for Advanced Study, Seoul, Republic of Korea. ⁴Department of Physics, Ewha Womans University, Seoul, Republic of Korea. ⁵Department of Physics, Harvard University, Cambridge, MA, USA. ⁶School of Physics and Astronomy, University of Minnesota, Minneapolis, MN, USA. ⁷Korea Electronics Technology Institute, Seongnam, Republic of Korea. ⁸Research Center for Electronic and Optical Materials, National Institute for Materials Science, Tsukuba, Japan. ⁹Research Center for Materials Nanoarchitectonics, National Institute for Materials Science, Tsukuba, Japan. ¹⁰Research Institute of Advanced Materials, Seoul National University, Seoul, Republic of Korea. ¹¹These authors contributed equally: Daesung Park, Changwon Park, Kunihiro Yananose. ✉e-mail: hand@kias.re.kr; hyobinyoo@snu.ac.kr

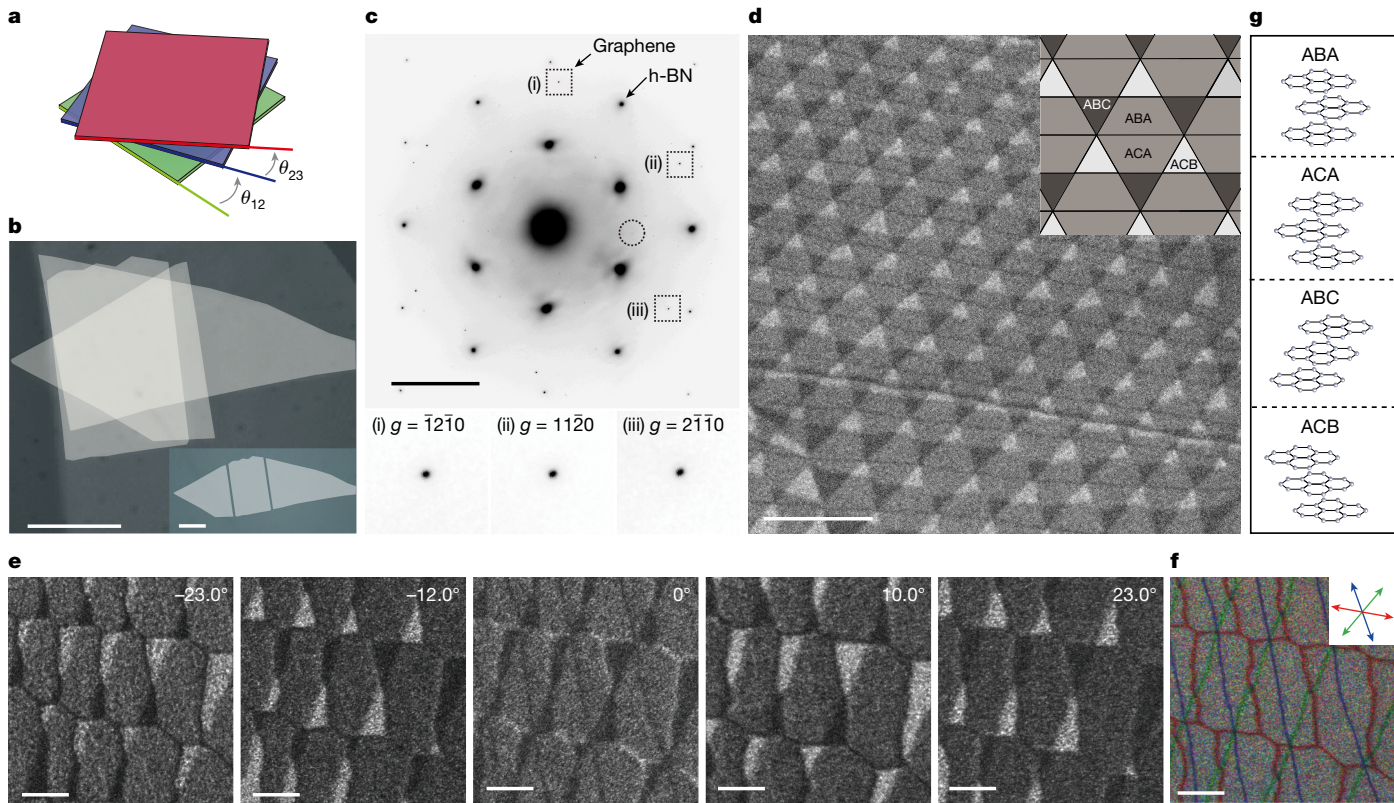


Fig. 1 | SSB atomic reconstruction in TTG. **a**, Schematic illustration of TTG. Note that θ_{12} and θ_{23} can have both positive and negative values. The same graphene layers are coloured differently to distinguish top, middle and bottom layers. **b**, Optical microscopy image of TTG. Monolayer graphene that was used to fabricate the TTG is shown in the inset. The monolayer graphene is segmented into three pieces before being stacked to fabricate TTG. Scale bars, 10 μm . **c**, SAED pattern obtained from TTG covered with h-BN layers. The $g = \bar{1}\bar{2}\bar{1}0$ Bragg peak is marked with a dashed circle and the $g = \bar{1}\bar{2}\bar{1}0$ (i), $g = 1\bar{1}\bar{2}0$ (ii) and $g = 2\bar{1}\bar{1}0$ (iii) Bragg peaks are marked with dashed squares, with their magnified views shown at the bottom. Scale bar, 5 nm^{-1} . **d**, DF TEM image of TTG with $\theta_{12} = 0^\circ$ and $\theta_{23} \approx 0.06^\circ$. The DF TEM image was acquired by taking the $g = \bar{1}\bar{2}\bar{1}0$ Bragg peak

marked by the dashed circle in **c**. Schematic representation of the domain structure with the corresponding stacking orders is shown in the inset. Scale bar, 500 nm. **e**, Tilt-series DF TEM images obtained from the TTG specimen with $\theta_{12} = 0^\circ$ and $\theta_{23} \approx 0.07^\circ$ by manipulating the tilt angle of the specimen in TEM (see details in Extended Data Fig. 1). Scale bar, 100 nm. **f**, Composite-colour DF TEM image obtained from the three sets of second-order Bragg peaks $g = \bar{1}\bar{2}\bar{1}0$, $g = 1\bar{1}\bar{2}0$ and $g = 2\bar{1}\bar{1}0$. Coloured lines indicate the domain walls, with the directions of the characteristic displacement vectors marked in the inset (see details in Extended Data Fig. 2). Scale bar, 100 nm. **g**, Schematic illustration of Bernal-stacked ABA and ACA configurations and rhombohedral-stacked ABC and ACB configurations.

stackings. In our work, we establish an optimal platform to explore the unique atomic reconstructions in TTG by controlling the twist angles near 0.1°, an order of magnitude smaller than previous works, to promote stronger reconstructions. Recognizing the presence of various competing stacking orders in TTG^{35–38}, we investigate the impact of the long-range interactions across entire layers on the restructuring behaviour, going beyond the typical emphasis on interactions limited to adjacent layers³⁹.

Atomic reconstruction in TTG

The structure of TTG was investigated by exploiting electron diffraction and dark-field (DF) imaging in TEM. We first fabricate the TTG specimen by controlling the two independent twist angles of θ_{12} and θ_{23} (Fig. 1a), using the cut-and-stack method reported previously^{10,40} (see Methods and Supplementary Information section 1 for details). Figure 1b shows an optical microscopy image of the marginally TTG (MTTG) covered with the hexagonal boron nitride (h-BN) layers. As shown in the selected area electron diffraction (SAED) pattern in Fig. 1c, we cannot distinguish several sets of Bragg peaks of the graphene layers, suggesting that the TTG specimen was successfully fabricated with the small enough twist angles (see Supplementary Information section 2 for details on twist-angle determination).

DF TEM imaging reveals the emergence of tessellated commensurate domains with their respective stacking orders resulting from atomic reconstruction. Observation of the $g = 10\bar{1}0$ DF TEM image (Fig. 1d) and its variations with the tilt angle of the sample (Fig. 1e) enables stacking-order identification within the commensurate domains (see Methods and Extended Data Fig. 1 for detailed diffraction analysis and Supplementary Information section 3 for atomic-scale image analysis). Similarly, the composite-colour DF TEM image obtained from the three sets of second-order Bragg peaks (Fig. 1f) reveals the configuration of domain walls and explains their corresponding lattice-shift vectors (see Methods, Extended Data Fig. 2 and Supplementary Information section 4 for details).

SSB in atomic reconstruction

Our DF TEM investigation on the MTTG specimen with $\theta_{12} = 0^\circ$ and $\theta_{23} \approx 0.06^\circ$ (Fig. 1d) reveals a regular arrangement of kagome-like domain lattice. It consists of six corner-sharing triangular domains surrounding inner hexagonal domains. These triangular domains alternate between rhombohedral ABC and ACB stackings (black and white regions in the inset of Fig. 1d), with the corresponding atomic models shown in Fig. 1g. Furthermore, we identified a 1D array of domain walls (dark lines in Fig. 1d and blue lines in Fig. 1f) within each inner hexagonal

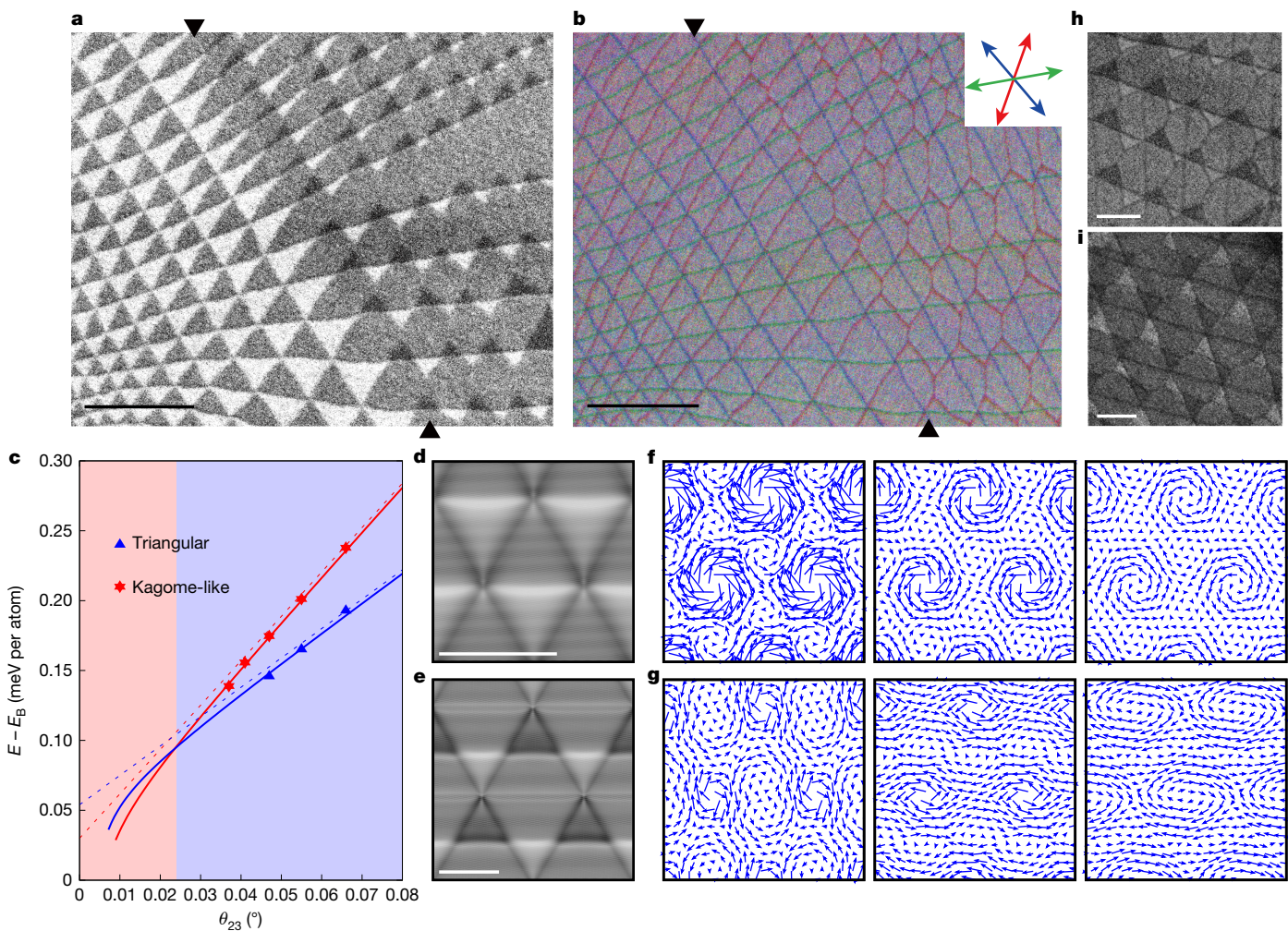


Fig. 2 | Structural phase transition in TTG. **a,b**, DF TEM images of TTG with $\theta_{12} = 0^\circ$ and $\theta_{23} \approx 0.1^\circ$. While the angle θ_{12} remained at 0° , θ_{23} gradually decreases from 0.14° (left) to 0.04° (right). $g = 1\bar{0}10$ DF TEM image (**a**) and composite-colour DF TEM image ($g = 1\bar{2}\bar{1}0$, $g = 11\bar{2}0$ and $g = 2\bar{1}\bar{1}0$; see detailed description in Extended Data Fig. 2) (**b**) are obtained from the same region of the specimen to exhibit domain and domain boundary contrast, respectively. Scale bars, 500 nm. **c**, The relative energies $E - E_B$ of TTG with varying θ_{23} while fixing $\theta_{12} = 0^\circ$. E_B is the energy of the Bernal-stacked trilayer graphene. Calculated configurations are plotted with blue triangles and red stars for the coloured triangular domain and kagome-like domain, respectively. Solid lines represent total energies including warping effects of domain boundaries and dashed lines represent them without the effects. The background colour variation points to the phase transition. **d,e**, Simulated BF TEM image of the coloured

triangular (**d**) and kagome-like (**e**) domains. Grey (black and white) area corresponds to Bernal (rhombohedral) stacking. Scale bars, 100 nm. **f,g**, The coarse-grained atomic displacements of triangular (**f**) and kagome (**g**) domains. The left, middle and right panels correspond to layers 3, 2 and 1, respectively. **h,i**, Composite DF TEM images of TTG obtained from region 1 with $\theta_{12} = 0.06^\circ$ and $\theta_{23} = 0^\circ$ (**h**) and region 2 with $\theta_{12} = 0^\circ$ and $\theta_{23} = 0.05^\circ$ of the same specimen (see the larger field-of-view image in Extended Data Fig. 3). The composite DF TEM image was obtained by summing $g = 1010$, $g = 1\bar{2}\bar{1}0$, $g = 11\bar{2}0$ and $g = 2\bar{1}\bar{1}0$ DF images to visualize the domain and domain boundary contrast together (see details in Extended Data Fig. 3). Note that the orientations of nematic orders observed in regions 1 and 2 are rotated 60° with respect to each other. Scale bars, 200 nm.

domain, distinctly separating two different Bernal ABA and ACA stackings (grey regions in the inset of Fig. 1d, with the corresponding atomic arrangements shown in Fig. 1g). The presence of a 1D array of domain walls inside the hexagonal domains reduces the original rotation symmetry of the MTTG, indicating the SSB characteristics of the atomic reconstruction process.

We investigate the impact of the twist-angle variations on the symmetry-breaking atomic reconstruction behaviour in MTTG. Despite achieving precise manipulation over the twist angle through the cut-and-stack method^{10,40}, inherent variations in the twist angle persist owing to limitations in control. In the MTTG specimen fabricated with $\theta_{12} = 0^\circ$ and $\theta_{23} \approx 0.1^\circ$, we observe a gradual change in the size of the moiré superlattice from left to right, with θ_{23} decreasing from 0.14° to 0.04° , whereas θ_{12} remained at 0° (Fig. 2a). We observe a sharp structural phase transition from triangular domain lattice (left)

to the kagome-like domain lattice (right) occurring at $\theta_{23} \approx 0.05^\circ$, with its boundary marked by the black triangles (Fig. 2a,b). Further analysis reveals that alternating Bernal and rhombohedral (grey and white coloured regions in Fig. 2a) stacking orders are formed in the triangular commensurate domains, exhibiting what we term ‘a coloured triangular domain lattice’. The transition from this lattice to the kagome-like domain lattice abruptly increases the prevalence of Bernal-stacked regions from approximately 50% to 75%, implying that the SSB in the reconstruction is related to the system favouring Bernal stacking over rhombohedral stacking.

Origins of structural phase transition

To understand the experimentally observed structural phase transition, we performed atomic force relaxations of a moiré unit cell using

Article

a newly developed interatomic potentials method^{27,28} (see Methods) to investigate the energetics of competing reconstruction patterns. Relative energies of the coloured triangular and the kagome-like domain lattices (blue triangles and red stars in Fig. 2c) with respect to the Bernal-stacked trilayer are plotted with varying θ_{23} while keeping θ_{12} at 0° . The simulated bright-field (BF) TEM image (see Methods for TEM image simulation) from the relaxed structures clearly shows alternations between Bernal and rhombohedral stacking orders for the coloured triangular lattice (Fig. 2d) and six-corner sharing triangular rhombohedral stacking domains with the inner hexagonal Bernal stacking domains divided by 1D domain walls (Fig. 2e), reproducing both experimental observations shown in Fig. 2a,b.

We note that the energies plotted for the two different lattice reconstructions increase linearly as the angle increases. This linear behaviour can be captured by considering the competition between energy gain by increasing the low-energy stacking area and simultaneous energy cost for domain-wall formation. For small twist angles, the energy can be written as $E(\theta_{23}) = \frac{A_B(\theta_{23})E_B + A_R(\theta_{23})E_R}{A_B(\theta_{23}) + A_R(\theta_{23})} + \gamma|\theta_{23}|$, in which $A_{B(R)}(\theta_{23})$ and $E_{B(R)}$ denote the angle-dependent area of Bernal (rhombohedral) stacked regions and their energies per unit area, respectively. We note that the first term in $E(\theta_{23})$ does not change with the angle unless the areal ratio between Bernal and rhombohedral stacking regions is altered with the angle and that the linear dependence on θ_{23} in the second term reflects the linearly increasing area-to-boundary ratio for each domain (see its derivation in Supplementary Information section 5). From the slopes of the energies plotted for the two relaxed structures, the constants γ for the coloured triangular and kagome domains can be estimated to be 621 and 1,013 meV per area of graphene unit cell, respectively. Then we can deduce that the phase transitions between the two domain lattices should occur when the two energy lines (blue and red lines in Fig. 2c) intersect at $\theta_k \approx 0.025^\circ$, which is consistent with the experimental observation of phase transition at $\theta_{23} \approx 0.05^\circ$ (Fig. 2a,b; see Supplementary Information sections 2 and 6 for details on determining θ_k). We note that the phase transition causes a discrete jump in the areal fraction of Bernal stacking, $\Delta A_B(\theta) = \frac{A_B(\theta)}{A_B(\theta) + A_R(\theta)}$, shifting from 50% to 75%.

Moreover, our theoretical investigation indicates that, as the angle θ_{23} decreases further below 0.01° , an alternative reconstruction pattern or warping effect of domain boundaries emerges, so that the whole area approaches the lowest-energy configuration of Bernal stacking (see Supplementary Information section 5 for details). As shown in Fig. 2c, the linear dependence of total energy does not hold if we consider distortion or warping of domain walls (see Supplementary Fig. 10 for pattern shapes). Therefore, for extremely small twist angles, two or three energetically degenerate domain patterns are possible.

Atomic reconstruction in the moiré systems involves rearrangement of atoms to maximize the area of lowest-energy stacking configuration at the cost of domain-wall formation^{5,7,8}. In TBG, for instance, the energy differences between Bernal (AB) stacking and unstable AA stacking are on the order of 10 meV per atom^{35–38} and, thus, on twisting two layers below about 1° , the entire region of the TBG specimen is dominated by Bernal-stacked domains with triangular networks of domain walls^{5,7,8}. With further decreasing angle, no further structural transition occurs in TBG because no other competing order exists. For trilayer graphene, however, there are two low-energy stacking orders, Bernal and rhombohedral types (Fig. 1g). Although their energy difference is on the order of 0.1 meV per atom, this minute energy difference turns out to be crucial for the formation of various periodic domain structures in MTTG. Alongside well-known factors such as twist angles and local strains^{5,7,8}, we find that the most decisive factor to determine moiré structures in MTTG is a small difference between total energies for Bernal and rhombohedral stacking orders. This emphasizes that a simple moiré-of-moiré framework is insufficient and that the long-range interlayer interactions across the entire layers should be considered properly.

We further investigate the driving mechanism for the structural phase transitions by inspecting local atomic displacement patterns. Figure 2f,g shows coarse-grained displacements of the coloured-triangular and kagome domain lattices, respectively. The left, middle and right panels correspond to the displacement maps for the top (layer number 3), middle (2) and bottom (1) layers, respectively. With varying θ_{23} and keeping $\theta_{12} = 0^\circ$, only the top layer is twisted with respect to the others. As shown in Fig. 2f, the local displacement vectors near the vertices of triangular domains form the same helical pattern for the bottom and middle layers, whereas it is reversed for the top layer with the twirling domain boundaries⁴¹. We also note that the local strains at the centres of triangular domains are negligible and that the bottom layer experiences less strains than the others. These strain patterns are similar to those shown in TBG^{5,7,8}. However, unlike TBG, the adjacent triangular domains in Fig. 2d have no choice but to form different stackings with slightly different energies, thereby distinguishing the coloured triangular domains in MTTG from simple triangular lattice in TBG.

On decreasing θ_{23} further, the atoms on the bottom layer overcome the local strain constraint imposed by the twisted top layer and are further relaxed to reduce the area of the rhombohedral domain by moving atoms along a specific direction (Fig. 2g). Such reconstruction results in uniaxial strain fields or SSB from the threefold rotational symmetry to the twofold one. As a result of this reconstruction, a kagome-like domain lattice with the nematic domain walls can be formed. This nematic boundary has three choices along three different diagonal directions of the hexagonal domain. We observe two instances of the kagome-like domain lattice exhibiting distinct directions for the nematic ordering in the different regions of the same specimen (Fig. 2h,i; see Extended Data Fig. 3 for a lower-magnification image), highlighting their SSB nature. Note that the orientations of the nematic domain walls observed in Fig. 2h,i are rotated by 60° relative to each other.

Complete structural phase diagram of TTG

MTTG presents a fertile ground for diverse domain patterns with different symmetries owing to the presence of the almost energetically equivalent yet different stacking orders. To investigate how the moiré superlattice domains manifest while independently varying the two twist angles θ_{12} and θ_{23} , we performed a comparative analysis between TEM imaging and simulations. A structural phase diagram of MTTG is presented in Fig. 3a. Our TEM observations are consistent with the simulated structures. Figure 3b,d shows experimental and simulated TEM domain contrast images, whereas Fig. 3c,e shows the corresponding domain boundary contrast images (see Extended Data Fig. 4 for the raw data). With the convention of twist angles defined in Fig. 1a, half of the first and second quadrants in $\theta_{12}-\theta_{23}$ space are enough to represent all possible twisting geometries (see discussion in Supplementary Information section 7). The first quadrant corresponds to helical stacking, whereas the second corresponds to alternated stacking. The colour scale in the diagram denotes the angle-dependent areal fraction of the Bernal-stacked region, $\Delta A_B(\theta) = \frac{A_B(\theta)}{A_B(\theta) + A_R(\theta)}$. The approximated expressions for energies of the various competing phases with the twist angles less than 0.1° can be found in Supplementary Information section 8.

In the TTG with alternated twist angles of the same magnitude ($\theta_{12} + \theta_{23} = 0$, marked with line 1 in Fig. 3a), ‘a simple triangular domain lattice’ emerges, in which Bernal-stacked domains of ABA and ACA alternate with each other (panels (i) of Fig. 3b–e), similar to TBG. Away from the line of $\theta_{12} + \theta_{23} = 0$, slight mismatch between the two twist angles generates moiré-of-moiré lattice. Our observation on TTG specimen with $\theta_{12} = -0.3^\circ$ and $\theta_{23} = 0.4^\circ$, in which the twist-angle combination deviates from $\theta_{12} + \theta_{23} = 0$, shows the simple triangular domain lattice surrounded by the hexagonal moiré-of-moiré domain-wall network (panels (ii) of Fig. 3b–e). In the case of incommensurate twist-angle

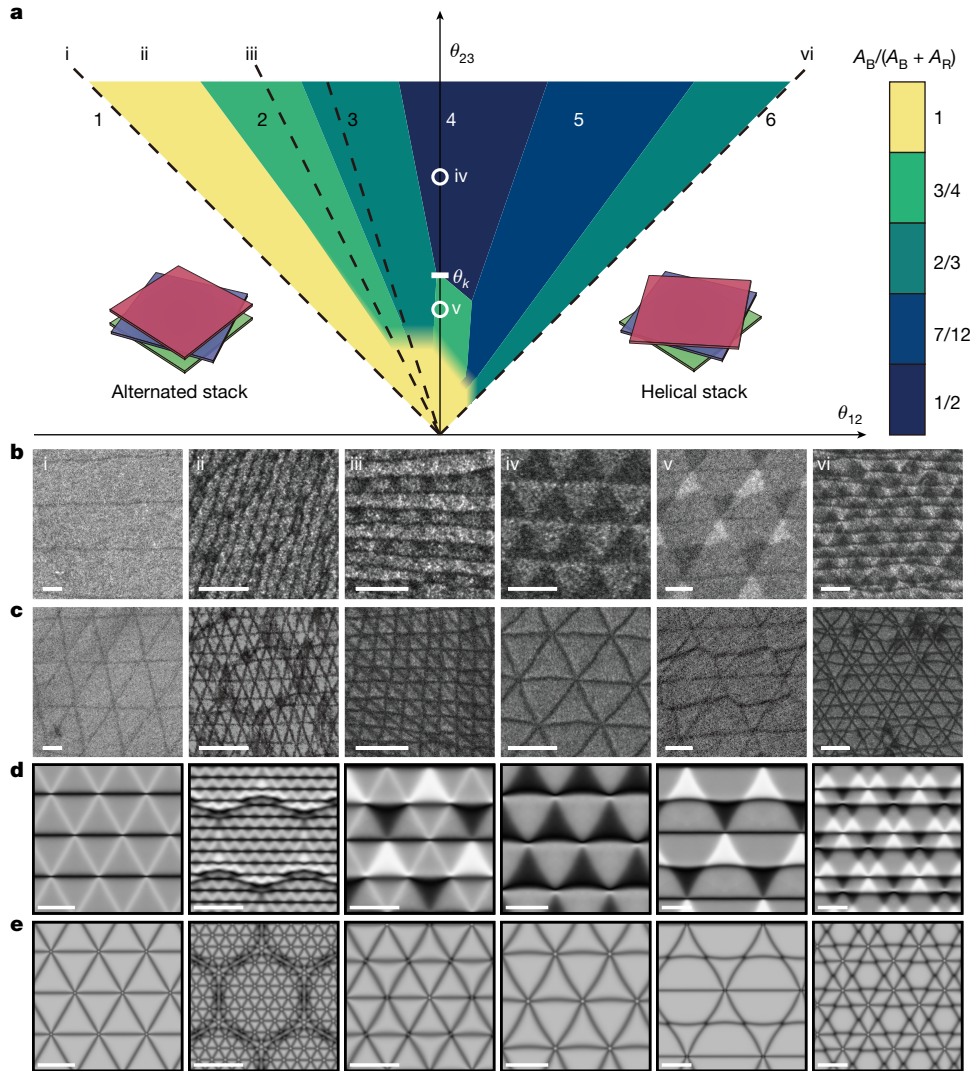


Fig. 3 | Structural phase diagram of TTG. **a**, The phase diagram drawn as a function of θ_{12} and θ_{23} . The colour scale indicates the normalized areal fraction of the Bernal-stacked region over the entire region, $\Delta A_B = \frac{A_B}{A_B + A_R}$, in which A_B and A_R denote the areas of the Bernal-stacked region and the rhombohedral-stacked region, respectively. The lines marked with Arabic numerals represent a series of commensurate conditions that is surrounded by distinct phases denoted by different colours: (1) $\theta_{12} + \theta_{23} = 0$; (2) $2\theta_{12} + \theta_{23} = 0$; (3) $3\theta_{12} + \theta_{23} = 0$; (4) $\theta_{12} = 0^\circ$; (5) $2\theta_{12} - \theta_{23} = 0$; and (6) $\theta_{12} - \theta_{23} = 0$. Experimentally observed phases are marked with roman numerals: (i) simple triangular domain lattice; (ii) simple triangular domain lattice bound by moiré-of-moiré boundaries; (iii) double-coloured triangular domain lattice; (iv) coloured triangular domain lattice; (v) kagome-like domain lattice; and (vi) hexagram domain lattice. Near 0° for both θ_{12} and θ_{23} , the transitions to $\Delta A_B = 1$ become continuous owing to warping effects, as indicated by the gradual colour changes. **b,c**, DF TEM images obtained for the experimentally observed phases with the corresponding twist angles of: (i) $\theta_{12} = -0.06^\circ$, $\theta_{23} = 0.06^\circ$; (ii) $\theta_{12} = -0.3^\circ$, $\theta_{23} = 0.4^\circ$; (iii) $\theta_{12} = -0.2^\circ$, $\theta_{23} = 0.4^\circ$; (iv) $\theta_{12} = 0^\circ$, $\theta_{23} = 0.09^\circ$; (v) $\theta_{12} = 0^\circ$, $\theta_{23} = 0.05^\circ$; and (vi) $\theta_{12} = 0.1^\circ$, $\theta_{23} = 0.1^\circ$. The first-order Bragg peak ($g = 10\bar{1}0$) (**b**) and the sum of the second-order Bragg peaks ($g = 1\bar{2}\bar{1}0$, $g = 1\bar{1}\bar{2}0$ and $g = 2\bar{1}\bar{1}0$) (**c**) are used to obtain DF TEM images to exhibit domain and domain boundary contrast, respectively (see Extended Data Fig. 4 for the raw data used to obtain domain boundary contrast images). **d,e**, Simulated DF TEM images obtained for phases (i)–(vi). Simulated DF TEM images exploiting the first-order Bragg peak (**d**) and the sum of the second-order Bragg peaks (**e**) reproduce the experimental observations shown in **b** and **c**. Scale bars, 100 nm.

combinations as in our observation, atomic reconstruction occurs at the two interfaces, forming locally commensurate lattice bound by the discommensurate boundaries^{2,21}. Depending on the details for morphologies of domain walls and twist angles, the resulting moiré-of-moiré domain-wall network can be hexagonal (panels (ii) of Fig. 3b–e) or triangular (see Supplementary Information section 9). Consequently, maximum areal fraction of Bernal stacking, $\Delta A_B = 1$, is maintained for a wide range of twist angles, as noted by the yellow-coloured region in Fig. 3a.

We note that there are discrete regions in the phase diagram in which the combinations of the two twist angles satisfy the commensurate conditions (see Supplementary Information section 10 for details). For instance, along the line of $2\theta_{12} + \theta_{23} = 0$ (marked with line 2 in Fig. 3a),

effects, as indicated by the gradual colour changes. **b,c**, DF TEM images obtained for the experimentally observed phases with the corresponding twist angles of: (i) $\theta_{12} = -0.06^\circ$, $\theta_{23} = 0.06^\circ$; (ii) $\theta_{12} = -0.3^\circ$, $\theta_{23} = 0.4^\circ$; (iii) $\theta_{12} = -0.2^\circ$, $\theta_{23} = 0.4^\circ$; (iv) $\theta_{12} = 0^\circ$, $\theta_{23} = 0.09^\circ$; (v) $\theta_{12} = 0^\circ$, $\theta_{23} = 0.05^\circ$; and (vi) $\theta_{12} = 0.1^\circ$, $\theta_{23} = 0.1^\circ$. The first-order Bragg peak ($g = 10\bar{1}0$) (**b**) and the sum of the second-order Bragg peaks ($g = 1\bar{2}\bar{1}0$, $g = 1\bar{1}\bar{2}0$ and $g = 2\bar{1}\bar{1}0$) (**c**) are used to obtain DF TEM images to exhibit domain and domain boundary contrast, respectively (see Extended Data Fig. 4 for the raw data used to obtain domain boundary contrast images). **d,e**, Simulated DF TEM images obtained for phases (i)–(vi). Simulated DF TEM images exploiting the first-order Bragg peak (**d**) and the sum of the second-order Bragg peaks (**e**) reproduce the experimental observations shown in **b** and **c**. Scale bars, 100 nm.

at which the ratio between the two moiré lengths becomes a rational number of 1/2, fully commensurate double-coloured triangular domain lattice is demonstrated (panels (iii) of Fig. 3b–e). In this configuration, the areal fraction of the Bernal-stacked region reduces to $\Delta A_B = 3/4$. Small deviation from the commensurate condition of $2\theta_{12} + \theta_{23} = 0$ forms larger-scale moiré-of-moiré domain walls with the corresponding areal fraction of the Bernal stacking, $\Delta A_B = 3/4$, preserved for a finite range of twist-angle combinations (Fig. 3a), as it does similarly near $\theta_{12} + \theta_{23} = 0$. Our theoretical investigation suggests more commensurate angle combinations (see Supplementary Information section 10 for details), including one denoted by the dashed line of $3\theta_{12} + \theta_{23} = 0$ (marked with line 3) surrounded by the areal fraction of Bernal stacking $\Delta A_B = 2/3$.

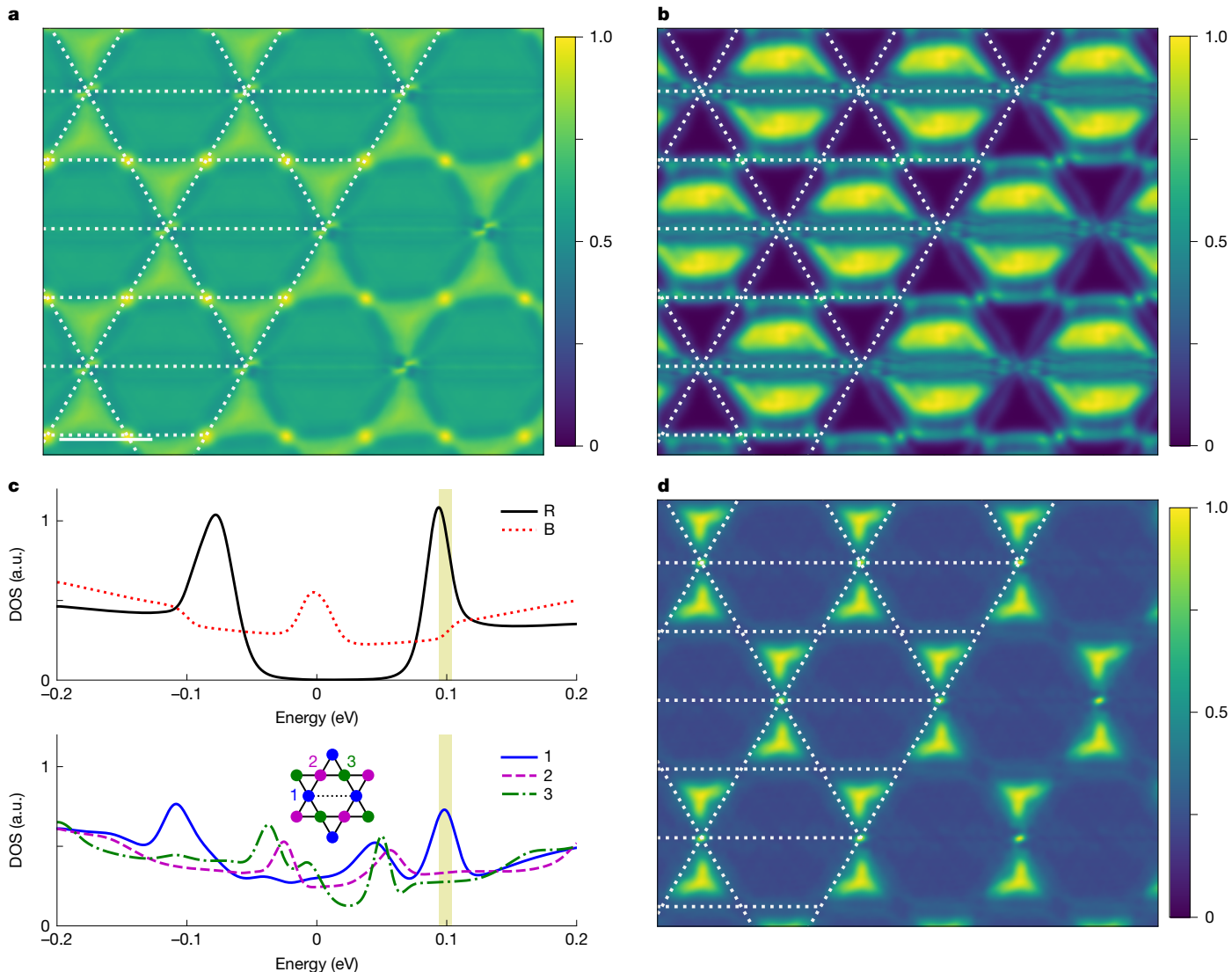


Fig. 4 | Electronic structures of kagome-like domain pattern. **a**, Spatial DOS for kagome-like domain lattice with $\theta_{12} = 0.08^\circ$ and $\theta_{23} = 0^\circ$ without perpendicular electric field. For DOS, we integrate the states of which energy is between -50 and 0 meV. The Fermi energy is set to be zero. For all DOS here the colour map is normalized to the maximum value and the dotted white lines are drawn to highlight the domain walls as a visual guide. Scale bar, 100 nm. **b**, Spatial DOS for kagome-like domain lattice near the Fermi level (from -10 to 0 meV) with the

finite perpendicular electric field. **c**, Energy-resolved DOS under the same electric field for rhombohedral (R) and Bernal (B) domains (top panel) and three different vertices (bottom panel; the positions of each vertex are indicated in the inset). To simulate a perpendicular field, we assign on-site energy shifts of $+0.1$, 0 and -0.1 eV for layers 1, 2 and 3, respectively. **d**, Spatial DOS of which energy is denoted by the shaded range in **c** with the finite electric field. a.u., arbitrary units.

As $|\theta_{12}|$ decreases at a fixed $\theta_{23} > \theta_k$, we find that the normalized ratio of Bernal-type stacking ΔA_B decreases stepwise from 1 to $3/4$, to $2/3$ and eventually to $1/2$ at $\theta_{12} \approx 0$ (marked with line 4 in Fig. 3a), as denoted by the different colours in Fig. 3a (see Extended Data Fig. 5 for the transition between the different phases). As both twist angles approach 0° , at which the stacking-energy contribution eventually dominates, we find that the areal fraction of Bernal stacking converges to 1 regardless of the pathway taken in the phase diagram. One such pathway involves a series of phase transitions or warping effects of boundaries, as denoted by the gradual colour changes in the phase diagram.

Last, in the first quadrant of the phase diagram, as θ_{12} increases to approach the line of $2\theta_{12} - \theta_{23} = 0$ (marked with line 5) and $\theta_{12} - \theta_{23} = 0$ (marked with line 6) at a fixed θ_{23} , the relaxed domain structures follow a similar physics to those near the lines of $2\theta_{12} + \theta_{23} = 0$ and $3\theta_{12} + \theta_{23} = 0$ on the second quadrant: two moiré lattices readjust themselves to form locally commensurate moiré domain structures with moiré-of-moiré domain walls. However, for the helical stacking cases, the two moiré

structures are inverted with respect to each other (see Supplementary Information section 10) so that the resulting super-domains show complicated coloured triangular lattices corresponding to different stacking orders. We also note that they can exhibit $\Delta A_B = 7/12$, differing from that of the alternated stacking cases. Notably, along $\theta_{12} - \theta_{23} = 0$, the relaxed domain shows a peculiar moiré superlattice with corner-shared hexagram-shaped units, still maintaining sixfold rotational symmetry (panels (vi) of Fig. 3b–e).

We emphasize that the total energy difference between Bernal and rhombohedral stackings (E_B and E_R) or, equivalently, the long-range interlayer interaction, is the most critical factor to determine relaxed domain patterns. As shown in Extended Data Fig. 6, the difference between E_B and E_R varies depending on the interlayer interactions between the first and third layers. By artificially controlling these interactions, we can relax the structures under two different energetic conditions, that is, $E_B < E_R$ and $E_B > E_R$. As shown in Extended Data Fig. 7, completely different relaxed results can be obtained for twist angles

corresponding to $\theta_{12} + \theta_{23} = 0$ and $\theta_{12} - \theta_{23} = 0$, thus highlighting a critical role of the long-range interactions in forming nontrivial superlattices (see comprehensive modelling in Supplementary Information section 11). We also note that, considering the inherent twist-angle inhomogeneity in TTG, unavoidable even with state-of-the-art techniques for fabricating twisted layered systems^{10,40,42}, sharp boundaries between disparate SSB structures could be possible in most of the MTG specimens, as illustrated in Fig. 2a and Extended Data Fig. 5.

Discussion and conclusions

Having provided a complete structural phase diagram of TTG with twist angles less than 0.1° , now we investigate its consequences for electronic properties. With typical domain sizes around the hundreds of nanometres scale observed in our work, electronic structures of TTG may be dominated by bulk electronic properties of domains and their boundaries. Under perpendicular electric fields, the rhombohedral-stacked region should open a bandgap, whereas the Bernal-stacked region maintains its metallic nature^{43,44}. Thus, we note that several phases shown in Fig. 3 can provide unique platforms on which various topological edge states can be realized when subjected to applied gate potentials. In the case of kagome-like domain lattices, for instance, diverse electronic states manifest at different junctions between distinct stacking orders. We note that the node region formed between two rhombohedral-stacked regions, that is, between ABC and ACB regions (shown in Fig. 1d and panel (v) of Fig. 3b), can host topological boundary states. With the applied perpendicular electric fields, both domains are fully gapped with distinct valley Chern numbers so that the topological boundary states develop as in TBG^{45–49} (see Supplementary Information section 12). Another type of the domain boundaries formed between two Bernal-stacked domains inside the hexagonal-shaped regions, on the contrary, does not host in-gap boundary states, as the two Bernal-stacked domains maintain their metallic nature. The other type of domain boundary is formed between rhombohedral-stacked and Bernal-stacked regions in which the valley Chern number cannot be determined well owing to metallic Bernal stacking^{46,50}. However, as shown by our electronic structure calculations (Supplementary Fig. 17), we find a resonant state between localized boundary states and metallic states on Bernal-stacked domains, suggesting the well-defined conducting channels along the boundaries in kagome-shaped domains.

Owing to disparate local stacking structures and notable boundary states between them as discussed above, the kagome-like domain lattice can host distinct electronic states (see Methods for electronic structure calculation). Without perpendicular electric field, local charge density indeed reflects different stacking geometries such that the rhombohedral stacking region has a higher density than the Bernal-stacked hexagonal area with clear nematic boundary and the increased charge density at vertices between triangular-shaped regions (Fig. 4a). With perpendicular electric field, all rhombohedral regions are fully gapped and all states at the Fermi energy are localized only in the Bernal-stacked area, as shown in Fig. 4b. We note that the triangular domain lattice shown in Fig. 2d can also show a similar variation in local electronic structure under the electric field, depending on stacking geometries³³ (see Supplementary Information section 13 for details). These localized states also clearly show the nematic characteristics indicated by the well-separating boundaries between two different Bernal-stacked regions. Notably, vertices have still in-gap states (Fig. 4c) and, as shown in Fig. 4d, the charge density near the band edge for the gapped rhombohedral state shows a peculiar array of dumbbell-shaped states at the triangular-shaped regions connected by the vertex boundary states. From these states, we note that the reconstructed domain lattices in TTG could provide a platform on which we predict intriguing interplays between various nontrivial correlated states, as spatially well-defined rhombohedral-stacked regions are separated by boundary states. The area of rhombohedral-stacked regions observed in several phases in

TTG seems to be large enough to maintain bulk electronic properties so that the superconducting⁵¹ and ferromagnetic states⁵² can be realized in each rhombohedral-stacked domain with appropriate doping and field controls. Then, we may consider an interesting interplay⁵³ between magnetic insulator and superconductor located side by side seamlessly across the domain walls in the reconstructed twisted layered systems.

Online content

Any methods, additional references, Nature Portfolio reporting summaries, source data, extended data, supplementary information, acknowledgements, peer review information; details of author contributions and competing interests; and statements of data and code availability are available at <https://doi.org/10.1038/s41586-025-08932-0>.

1. Frenkel, Y. I. & Kontorova, T. The model of dislocation in solid body. *Zh. Eksp. Teor. Fiz.* **8**, 1340–1348 (1938).
2. McMillan, W. L. Theory of discommensurations and the commensurate-incommensurate charge-density-wave phase transition. *Phys. Rev. B* **14**, 1496–1502 (1976).
3. Aubry, S. & André, G. Analyticity breaking and Anderson localization in incommensurate lattices. *Ann. Israel Phys. Soc.* **3**, 18 (1980).
4. Bak, P. Commensurate phases, incommensurate phases and the devil's staircase. *Rep. Prog. Phys.* **45**, 587 (1982).
5. Alden, J. S. et al. Strain solitons and topological defects in bilayer graphene. *Proc. Natl. Acad. Sci. USA* **110**, 11256–11260 (2013).
6. Huang, F.-T. & Cheong, S.-W. Aperiodic topological order in the domain configurations of functional materials. *Nat. Rev. Mater.* **2**, 17004 (2017).
7. Yoo, H. et al. Atomic and electronic reconstruction at the van der Waals interface in twisted bilayer graphene. *Nat. Mater.* **18**, 448–453 (2019).
8. Engelke, R. et al. Topological nature of dislocation networks in two-dimensional moiré materials. *Phys. Rev. B* **107**, 125413 (2023).
9. Zhu, Z., Carr, S., Massatt, D., Luskin, M. & Kaxiras, E. Twisted trilayer graphene: a precisely tunable platform for correlated electrons. *Phys. Rev. Lett.* **125**, 116404 (2020).
10. Hao, Z. et al. Electric field-tunable superconductivity in alternating-twist magic-angle trilayer graphene. *Science* **371**, 1133–1138 (2021).
11. Park, J. M., Cao, Y., Watanabe, K., Taniguchi, T. & Jarillo-Herrero, P. Tunable strongly coupled superconductivity in magic-angle twisted trilayer graphene. *Nature* **590**, 249–255 (2021).
12. Zhang, X. et al. Correlated insulating states and transport signature of superconductivity in twisted trilayer graphene superlattices. *Phys. Rev. Lett.* **127**, 166802 (2021).
13. Shin, J., Chittari, B. L. & Jung, J. Stacking and gate-tunable topological flat bands, gaps, and anisotropic strip patterns in twisted trilayer graphene. *Phys. Rev. B* **104**, 045413 (2021).
14. Turkel, S. et al. Orderly disorder in magic-angle twisted trilayer graphene. *Science* **376**, 193–199 (2022).
15. Park, J. M. et al. Robust superconductivity in magic-angle multilayer graphene family. *Nat. Mater.* **21**, 877–883 (2022).
16. Li, Y. et al. Symmetry breaking and anomalous conductivity in a double-moiré superlattice. *Nano Lett.* **22**, 6215–6222 (2022).
17. Kim, H. et al. Evidence for unconventional superconductivity in twisted trilayer graphene. *Nature* **606**, 494–500 (2022).
18. Lin, X., Li, C., Su, K. & Ni, J. Energetic stability and spatial inhomogeneity in the local electronic structure of relaxed twisted trilayer graphene. *Phys. Rev. B* **106**, 075423 (2022).
19. Devakul, T. et al. Magic-angle helical trilayer graphene. *Sci. Adv.* **9**, eadi6063 (2023).
20. Kim, H. et al. Imaging inter-valley coherent order in magic-angle twisted trilayer graphene. *Nature* **623**, 942–948 (2023).
21. Nakatsuji, N., Kawakami, T. & Koshino, M. Multiscale lattice relaxation in general twisted trilayer graphenes. *Phys. Rev. X* **13**, 041007 (2023).
22. Uri, A. et al. Superconductivity and strong interactions in a tunable moiré quasicrystal. *Nature* **620**, 762–767 (2023).
23. Mao, Y., Guerci, D. & Mora, C. Supermoiré low-energy effective theory of twisted trilayer graphene. *Phys. Rev. B* **107**, 125423 (2023).
24. Popov, F. K. & Tarnopolsky, G. Magic angles in equal-twist trilayer graphene. *Phys. Rev. B* **108**, L081124 (2023).
25. Meng, H., Zhan, Z. & Yuan, S. Commensurate and incommensurate double moiré interference in twisted trilayer graphene. *Phys. Rev. B* **107**, 035109 (2023).
26. Craig, I. M. et al. Local atomic stacking and symmetry in twisted graphene trilayers. *Nat. Mater.* **23**, 323–330 (2024).
27. Park, C. Calculation of charge density wave phase diagram by interacting eigenmodes method. *J. Phys. Condens. Matter* **34**, 315401 (2022).
28. Park, C. & Son, Y.-W. Condensation of preformed charge density waves in kagome metals. *Nat. Commun.* **14**, 7309 (2023).
29. Kim, K. et al. Tunable moiré bands and strong correlations in small-twist-angle bilayer graphene. *Proc. Natl. Acad. Sci. USA* **114**, 3364–3369 (2017).
30. Cao, Y. et al. Correlated insulator behaviour at half-filling in magic-angle graphene superlattices. *Nature* **556**, 80–84 (2018).
31. Cao, Y. et al. Unconventional superconductivity in magic-angle graphene superlattices. *Nature* **556**, 43–50 (2018).
32. Zondiner, U. et al. Cascade of phase transitions and Dirac revivals in magic-angle graphene. *Nature* **582**, 203–208 (2020).

33. Zhang, S. et al. Domino-like stacking order switching in twisted monolayer–multilayer graphene. *Nat. Mater.* **21**, 621–626 (2022).
34. Khalaf, E., Kruchkov, A. J., Tarnopolsky, G. & Vishwanath, A. Magic angle hierarchy in twisted graphene multilayers. *Phys. Rev. B* **100**, 085109 (2019).
35. Lipson, H. S. & Stokes, A. The structure of graphite. *Proc. R. Soc. Lond. A. Math. Phys. Sci.* **181**, 101–105 (1942).
36. Boehm, H. P. & Coughlin, R. W. Enthalpy difference of hexagonal and rhombohedral graphite. *Carbon* **2**, 1–6 (1964).
37. Li, H. et al. Global control of stacking-order phase transition by doping and electric field in few-layer graphene. *Nano Lett.* **20**, 3106–3112 (2020).
38. Nery, J. P., Calandra, M. & Mauri, F. Ab-initio energetics of graphite and multilayer graphene: stability of Bernal versus rhombohedral stacking. *2D Mater.* **8**, 035006 (2021).
39. Kolmogorov, A. N. & Crespi, V. H. Registry-dependent interlayer potential for graphitic systems. *Phys. Rev. B* **71**, 235415 (2005).
40. Saito, Y., Ge, J., Watanabe, K., Taniguchi, T. & Young, A. F. Independent superconductors and correlated insulators in twisted bilayer graphene. *Nat. Phys.* **16**, 926–930 (2020).
41. Kaliteevski, M. A., Enaldiev, V. & Fal'ko, V. I. Twirling and spontaneous symmetry breaking of domain wall networks in lattice-reconstructed heterostructures of two-dimensional materials. *Nano Lett.* **23**, 8875–8880 (2023).
42. Uri, A. et al. Mapping the twist-angle disorder and Landau levels in magic-angle graphene. *Nature* **581**, 47–52 (2020).
43. Lu, C., Chang, C.-P., Huang, Y.-C., Chen, R.-B. & Lin, M. Influence of an electric field on the optical properties of few-layer graphene with AB stacking. *Phys. Rev. B* **73**, 144427 (2006).
44. Aoki, M. & Amawashi, H. Dependence of band structures on stacking and field in layered graphene. *Solid State Commun.* **142**, 123–127 (2007).
45. Martin, I., Blanter, Y. M. & Morpurgo, A. Topological confinement in bilayer graphene. *Phys. Rev. Lett.* **100**, 036804 (2008).
46. Zhang, F., MacDonald, A. H. & Mele, E. J. Valley Chern numbers and boundary modes in gapped bilayer graphene. *Proc. Natl Acad. Sci. USA* **110**, 10546–10551 (2013).
47. San-Jose, P. & Prada, E. Helical networks in twisted bilayer graphene under interlayer bias. *Phys. Rev. B* **88**, 121408 (2013).
48. Huang, S. et al. Topologically protected helical states in minimally twisted bilayer graphene. *Phys. Rev. Lett.* **121**, 037702 (2018).
49. Tsim, B., Nam, N. N. T. & Koshino, M. Perfect one-dimensional chiral states in biased twisted bilayer graphene. *Phys. Rev. B* **101**, 125409 (2020).
50. Zou, K., Zhang, F., Clapp, C., MacDonald, A. & Zhu, J. Transport studies of dual-gated ABC and ABA trilayer graphene: band gap opening and band structure tuning in very large perpendicular electric fields. *Nano Lett.* **13**, 369–373 (2013).
51. Zhou, H., Xie, T., Taniguchi, T., Watanabe, K. & Young, A. F. Superconductivity in rhombohedral trilayer graphene. *Nature* **598**, 434–438 (2021).
52. Zhou, H. et al. Half- and quarter-metals in rhombohedral trilayer graphene. *Nature* **598**, 429–433 (2021).
53. Sau, J. D., Lutchyn, R. M., Tewari, S. & Das Sarma, S. Generic new platform for topological quantum computation using semiconductor heterostructures. *Phys. Rev. Lett.* **104**, 040502 (2010).

Publisher's note Springer Nature remains neutral with regard to jurisdictional claims in published maps and institutional affiliations.

Springer Nature or its licensor (e.g. a society or other partner) holds exclusive rights to this article under a publishing agreement with the author(s) or other rightsholder(s); author self-archiving of the accepted manuscript version of this article is solely governed by the terms of such publishing agreement and applicable law.

© The Author(s), under exclusive licence to Springer Nature Limited 2025

Methods

Sample fabrication

TTG was fabricated by using the cut-and-stack method^{10,40} (see Supplementary Information section 1 for details). We cut the monolayer graphene into three pieces by using the contact mode of atomic force microscopy (AFM) to precisely control the twist angle between each layer. Specifically, we conducted a line scan using a conductive atomic force microscopy tip while applying the a.c. voltage. We used a worn atomic force microscope tip during the cutting process to widen the pre-cut line width of the graphene flake, which aids in aligning the h-BN with the graphene flake. The AFM conditions for cutting the monolayer graphene are as follows. (1) The type of cantilever tip in AFM is a Pt/Cr-coated conductive tip (Multi75E-G, BudgetSensors). (2) The magnitude of the tip loading force is about 60–90 nN. (3) The scan rate is 0.5 Hz. (4) The amplitude and frequency of the a.c. voltage are 30 V and 100 kHz, respectively. The next step involves manufacturing a stamp that consists of poly(bisphenol A carbonate) coated on polydimethylsiloxane (PDMS). In a sequential process, we lift h-BN and three graphene pieces onto the stamp, carefully adjusting the twist angles. We used an engagement angle of approximately 3° between the stamp and each flake during the sample fabrication process. To avoid potential structural rearrangement between the graphene and the h-BN layer, we deliberately offset the graphene from the top h-BN layer using the straight edges of the flakes. This offset angle is set to be greater than 3° to prevent closer alignment that could lead to such rearrangement⁵⁴. Finally, we increase the temperature up to 180 °C and transfer the TTG fabricated on h-BN to a 20-nm-thick SiN membrane chip. See Supplementary Information section 1 for details on the fabrication steps.

TEM experiment

We use the 80-kV and 200-kV field emission gun transmission electron microscope (JEM-2100F, JEOL) equipped with a CMOS camera (OneView, Gatan) to obtain SAED patterns and DF TEM images. Owing to the limitations in angular resolution in SAED in reciprocal space and the spatial resolution of DF TEM imaging in real space, we rely on SAED patterns for resolving twist angles larger than 0.3° and on DF TEM images for resolving twist angles smaller than 0.3°. To estimate the twist angle from the moiré length λ_m , according to the relation $\lambda_m = a / (2 \sin \theta / 2)$, in which a is the lattice constant of graphene, we measure and average the edge lengths of the moiré superlattice from DF TEM images obtained using the second-order Bragg peaks. The hexagonal unit cell resolved by the DF TEM images is divided into two triangular half-unit cells and the three edge lengths of each half-unit cell are averaged to estimate λ_m for each half-unit cell. We note that the experimental measurements to estimate the twist angle were performed on moiré domains in which strain effects are minimized, with distortions in the moiré unit cell limited to edge-length variations of less than 30%. This allows for reliable comparison with theoretical estimation based on an ideal moiré superlattice (see Supplementary Information sections 2 and 6 for details).

For the DF TEM imaging, we used an aperture in the diffraction plane to isolate various types of Bragg peak (denoted as g). Depending on the Bragg peak we exploit, diverse spatial maps can be generated, for which each map provides distinct crystallographic information. We used an objective aperture with a diameter of 0.68 nm⁻¹ to select specific Bragg peaks. The electron dose rate used in our study was approximately 10³ e⁻ (nm² s)⁻¹ and the exposure time to take the DF TEM image ranges from 10 to 60 s. A double-tilt holder was used to control the tilt angle of the specimen in the microscope. Starting by aligning the specimen with the [0001] zone axis, we capture a series of DF TEM images using the first-order Bragg peak ($g = 1\bar{0}0$) while continuously changing the tilt angle of the specimen. By counting the amount of electrons obtained from each domain region, we plot the intensity

variation as illustrated in Extended Data Fig. 1c. These sinusoidal trends are generated by the interference of scattered electrons emanating from each layer in the TTG, containing 3D structural information^{5,55–58}. Analysing the diffraction intensity variation as a function of the specimen tilt angle, the atomic registry of the domain formed within the TTG can be identified. Also, we use the DF TEM imaging with the second-order Bragg peaks to distinguish the lattice-shift vector associated with each domain boundary⁵⁸. After acquiring three different sets of DF TEM images using second-order Bragg peaks ($g = 1\bar{2}\bar{1}0$, $g = 1\bar{1}\bar{2}0$ and $g = 2\bar{1}\bar{1}0$), we colour-adjust the contrast of the three images with red, green and blue colours. By summing those three colour-adjusted images, we obtain the composite-colour DF TEM images that visualize domain boundaries (Figs. 1f and 2b and Extended Data Fig. 2e), which are colour-coded according to the lattice-shift vectors. See Extended Data Fig. 2 and Supplementary Information section 4 for details. Spherical aberration (c_s) corrected annular DF scanning TEM (Themis Z, Thermo Fisher Scientific) was used to directly visualize the stacking orders within the domains. An acceleration voltage of 80 kV was used, along with a probe convergence angle of 27 mrad and collection angles of 42 mrad (inner) and 200 mrad (outer).

TEM simulation

For each optimized atomic structure, the simulated DF TEM image is obtained from the diffraction intensity I at pixel \mathbf{r} as $I(\mathbf{r}) = |\sum_j \exp[i(\mathbf{r} - \mathbf{R}_j) \times (\mathbf{k}_o - \mathbf{k}_i)]|^2$, in which \mathbf{k}_i and \mathbf{k}_o are wavevectors of incident and elastically scattered electron beams satisfying $|\mathbf{k}_i| = |\mathbf{k}_o|$ and \mathbf{R}_j is a position vector of atom j . The summation is done for atoms in a cylinder centred at \mathbf{r} with a radius 12 Å and tilted by incident angle θ_{in} . Because the relative in-plane displacements of atoms are very small within the cylinder, $I(\mathbf{r})$ is sharply peaked at $\mathbf{k}_o = \mathbf{k}_i + \mathbf{G}_{||} + \Delta k_z \hat{\mathbf{z}}$, in which $\mathbf{G}_{||}$ is the reciprocal vector of a monolayer graphene and $\Delta k_z \hat{\mathbf{z}}$ is the change of wavevector along the out-of-plane direction of $\hat{\mathbf{z}}$. For $|\mathbf{k}_i| \gg |\mathbf{G}_{||}|$, which is the situation for the usual DF TEM set-up, the elastic scattering condition becomes $\mathbf{k}_i \times \mathbf{G}_{||} = -\mathbf{k}_i \times \Delta k_z \hat{\mathbf{z}}$. Specifically, when the in-plane component of \mathbf{k}_i is parallel to $\mathbf{G}_{||}$, $\Delta k_z = |\mathbf{G}_{||}| \tan \theta_{in}$ and the diffraction intensity at $\mathbf{G}_{||}$ for an untwisted n -layer graphene becomes $I(\mathbf{r}; \mathbf{G}_{||}) = |\sum_{k=1}^n \exp[i \mathbf{t}_k \times \mathbf{G}_{||} + d |\mathbf{G}_{||}| \tan \theta_{in}]|^2$, in which \mathbf{t}_k is the overall translation of the k th layer and d is the interlayer distance. Simulated BF TEM images are obtained from the transmittance of an electron beam, which is approximately calculated for each unit cell as the area of the unit cell subtracted with the projected area of atomic spheres of radius 0.5 Å. Here the direction of projection is given by θ_{in} . For maximum contrast between Bernal stacking and rhombohedral stacking areas, θ_{in} is set to be $d \tan \theta_{in} = 0.81$ and 1.70 Å for DF TEM and BF TEM simulations, respectively. For second-order Bragg peak simulations, θ_{in} is set to be zero for the intensities of the Bernal (rhombohedral) stacking area and the brightest domain boundary to be the same.

Interatomic potentials for lattice relaxations

Our simulation method is designed to reproduce ab initio calculation results in molecular dynamics for very large systems accurately and can describe complex potential landscapes for delicate structural phase transitions in various materials reliably^{27,28}. To describe interlayer interactions, we add the pairwise interaction from the Kolmogorov-Crespi (KC) potential³⁹. Even though the binding energies of various stacking geometries in TBG are well captured by the KC potential³⁹, we found that its naive application to trilayer graphene results in an erroneous preference for rhombohedral stacking over Bernal stacking by 2.634 meV nm⁻². This is in contrast to experiment^{35–37} and first-principles calculations³⁸ pointing to the Bernal stacking as the ground state of trilayer graphene. Therefore we modify the KC potential to reflect the small energetic gain of Bernal stacking over rhombohedral stacking by adding a further long-ranged interlayer interaction between the topmost and bottommost layers in the trilayer.

Article

Our interatomic potential is the sum of intralayer and interlayer potential by treating them independently. Thanks to the enormous elastic constants of graphene, the maximum strain of twisted graphene layers is estimated to be less than 1% from our calculations, so we can safely neglect anharmonic effects. Also, by exploiting the fact that no bonds between carbon atoms break or wildly alter during the optimization, the computational cost can be further reduced and straightforwardly parallelized to relax about ten million atoms. The harmonic intralayer potential can be readily obtained from the phonon dispersion relation of monolayer graphene. For the reference phonon calculation, we have used density functional perturbation theory⁵⁹ with the generalized gradient approximation for the exchange-correlation functional⁶⁰. For interlayer potentials, we have used the pairwise interatomic potential developed by Kolmogorov and Crespi (KC potential)³⁹ that distinguishes energetic differences depending on the registry between two graphene layers. Because the corrugations in TTG are negligibly small, the KC potential between two carbon atoms on different layers connected by $\mathbf{r} = (x, y, z)$ can be written as $V(\mathbf{r}) = e^{-\lambda(r-z_0)}[C + 2f(r_{||})] - A(r/z_0)^{-6}$, in which $r = |\mathbf{r}|$, $r_{||}^2 = r^2 - z^2$ and $f(r_{||}) = e^{-(r_{||}/\delta)^2} \sum_{n=0} \infty C_{2n} (r_{||}/\delta)^{2n}$. We use a set of parameters following a previous work³⁹, $\lambda = 3.629 \text{ \AA}^{-1}$, $z_0 = 3.34 \text{ \AA}$, $A = 10.238$, $\delta = 0.578 \text{ \AA}$, $C_0 = 15.71$, $C_2 = 12.29$ and $C_4 = 4.993$ and the potential has units meV. With these equations applied to interlayer interactions between the bottom and middle layers and to those between the middle and top layers, respectively, the rhombohedral trilayer graphene is energetically favoured over the Bernal trilayer graphene by 0.023 meV per atom or 2.634 meV nm⁻². This is because of a tiny, spurious, alternating out-of-plane displacement (less than 0.1% of the interlayer distance) for nearest interlayer carbon atoms denoted by the red arrows in Extended Data Fig. 6a,b. To correct the ground-state configuration to be Bernal type, we introduce a simple Gaussian potential between the top and bottom layers, $V_{2nn}(\mathbf{r}) = -V e^{-3(|\mathbf{r}|^2 - z^2)} = -V e^{-3r_{||}^2}$, as shown in Extended Data Fig. 6c. With $V_{2nn}(\mathbf{r})$, the difference between the energy of Bernal stacking (E_B) and one of rhombohedral stacking (E_R) can be linearly tunable, as shown in Extended Data Fig. 6d. We set $V = 0.5 \text{ meV}$ corresponding to $E_B - E_R = -0.06 \text{ meV}$ per atom to reproduce the experimental structural phase transition between triangular and kagome-shaped phases. We checked that the details of correcting Gaussian potential hardly change the energy configurations. For example, we confirmed that doubling the width of our Gaussian potential changes the total energy of kagome patterns by less than 0.01 meV per atom.

Estimation of domain-wall energies

There are two distinct domain walls in TTG. One boundary is in between two Bernal-stacked regions (type 1) and the other is in between Bernal and rhombohedral stacking regions (type 2), as shown in Extended Data Fig. 8a,b, respectively. As shown in Extended Data Fig. 8c, the corrugations in the top and bottom layers along the type 1 domain wall are symmetric with respect to the flat middle layer. Unlike the symmetric type 1 domain wall, the corrugations along the type 2 domain wall in Extended Data Fig. 8d are asymmetric such that the corrugation on the top layer is induced from that of the middle layer with much smaller amplitudes than that of the type 1 domain wall. Simultaneously, the bottom layer distorts less than the corresponding type 1 wall. Because the domain-wall energy mainly comes from the curvature of corrugations, we expect that the domain-wall energy of type 1 could be larger than that of type 2. Because the energy of TTG at small angles linearly depends on the scaling of both twist angles as shown in Extended Data Fig. 8e, we can extract the energy of the domain wall from the slope of the energy on the twist angle. Counting the total length of the domain wall per moiré unit cell, the calculated wall energies are 137 and 84 meV Å⁻¹ for type 1 and 2 domain walls, respectively. In a similar way, we can also compute moiré-of-moiré domain walls from atomistic simulations based on interatomic potentials.

Electronic structure calculations

We use the spinless tight-binding approximation with one p_z orbital for each carbon atom. The matrix element between the i th and j th atoms in the Hamiltonian matrix at a crystal moment \mathbf{k} is given as $H_{ij}(\mathbf{k}) = \sum_{\mathbf{R}} t_{ij\mathbf{R}} \exp(i\mathbf{k} \times \mathbf{R})$, in which \mathbf{R} is the lattice translation vector. For the interlayer and intralayer hoppings, we used $t_{ij\mathbf{R}} = t(r) = n^2 V_{ppp}(r) + (1 - n^2) V_{ppm}(r)$ following a previous work⁶¹, in which $r = |\mathbf{r}_{ij\mathbf{R}}| = |\mathbf{r}_j - \mathbf{r}_i + \mathbf{R}|$ is the distance between atoms i and j and $n = z/r$ is the z -direction cosine of $\mathbf{r}_{ij\mathbf{R}}$. Each exponentially decaying Slater-Koster parameter is given by $V_{ppm}(r) = -\gamma_0 \exp[q_{\pi}(1 - r/a_{\pi})]$ and $V_{ppp}(r) = \gamma_1 \exp[q_{\pi}(1 - r/a_{\pi})]$ inside the cut-off radius $r_{\text{cut}} = 5 \text{ \AA}$ for the interlayer hopping and we only consider the nearest-neighbour bonds for the intralayer hopping, at which $\gamma_0 = 2.7 \text{ eV}$, $\gamma_1 = 0.48 \text{ eV}$, $a_{\pi} = 1.418 \text{ \AA}$, $a_o = 3.349 \text{ \AA}$ and $q_{\pi}/a_{\pi} = q_o/a_o = 2.218 \text{ \AA}^{-1}$. The applied electric field perpendicular to the layer is included by setting the on-site energy difference between the layers: $+\Delta U = 0.1 \text{ eV}$ for the top layer, 0 eV for the middle layer and $-\Delta U$ for the bottom layer, respectively. We consider a specific kagome-like domain lattice TTG with $\theta_{12} = 0.083^\circ$ and $\theta_{23} = 0^\circ$ that includes 2,887,206 carbon atoms in the moiré unit cell with its lattice constant of $1,706.13 \text{ \AA}$. We investigated the electronic structures near the Fermi level by using the ARPACK eigenvalue solver based on the implicitly restarted Lanczos method⁶². Also, the PETSc library is used as the linear equation solver for the shift-invert mode⁶³. Density of states (DOS) were calculated by the Gaussian broadening of energy eigenvalues with $\sigma = 6 \text{ meV}$. We confirmed that the DOS were sufficiently converged at 4×4 gamma-centred momentum space grid. Also, site-projected DOS were evaluated from the weight of orbitals belonging to each site.

Data availability

The data that support the findings of this study are presented in the paper, Extended Data and Supplementary Information. Any other relevant data are available from the corresponding authors on request.

54. Woods, C. R. et al. Commensurate–incommensurate transition in graphene on hexagonal boron nitride. *Nat. Phys.* **10**, 451–456 (2014).
55. Meyer, J. C. et al. The structure of suspended graphene sheets. *Nature* **446**, 60–63 (2007).
56. Brown, L. et al. Twinning and twisting of tri- and bilayer graphene. *Nano Lett.* **12**, 1609–1615 (2012).
57. Sung, S. H., Schnitzer, N., Brown, L., Park, J. & Hovden, R. Stacking, strain, and twist in 2D materials quantified by 3D electron diffraction. *Phys. Rev. Mater.* **3**, 064003 (2019).
58. Lin, J. et al. AC/AB stacking boundaries in bilayer graphene. *Nano Lett.* **13**, 3262–3268 (2013).
59. Baroni, S., de Gironcoli, S., Dal Corso, A. & Giannozzi, P. Phonons and related crystal properties from density-functional perturbation theory. *Rev. Mod. Phys.* **73**, 515 (2001).
60. Perdew, J. P., Burke, K. & Ernzerhof, M. Generalized gradient approximation made simple. *Phys. Rev. Lett.* **77**, 3865 (1996).
61. Trambly de Laissardière, G., Mayou, D. & Magaud, L. Localization of Dirac electrons in rotated graphene bilayers. *Nano Lett.* **10**, 804–808 (2010).
62. OpenCollab. ARPACK-ng: high-performance eigenvalue solver for large sparse matrices. GitHub <https://github.com/opencollab/arpack-ng> (2023).
63. Balay, S., Gropp, W. D., McInnes, L. C. & Smith, B. F. in *Modern Software Tools for Scientific Computing* (eds Arge, E., Bruaset, A. M. & Langtangen, H. P.) 163–202 (Springer, 1997).

Acknowledgements D.P., B.K. and H.Y. were supported by the National Research Foundation of Korea (NRF) (grant no. RS-2021-NR061606). H.Y. was supported by the NRF (grant nos. RS-2021-NR060087 and NRF-2022R1A4A1033562) and POSCO Science Fellowship of POSCO TJ Park Foundation. C.P. was supported by the new generation research programme (CG079701) at Korea Institute for Advanced Study (KIAS). E.K. was supported by a KIAS individual grant (CG075002). K.Y. was supported by a KIAS individual grant (CG092501). Y.-W.S. was supported by the KIAS individual grant (CG031509). TEM work was supported by the Center for Materials Analysis at Research Institute of Advanced Materials (RIAM), Seoul National University and the Center for Nano Materials at Sogang University. Computations were supported by the Center for Advanced Computation of KIAS. X.Z., K.D., M.G. and K. Wang were supported by NSF DMREF award 1922165. H.-M.K., S.-G.K. and H.K. acknowledge support from Material Innovation Leading Project through the NRF financed by the Ministry of Science and ICT (2020M3H4A3081879). S.M.Y. was supported by the NRF (grant no. RS-2023-NR076385). P.K. acknowledges the support from DOE (DE-SC0012260) for sample preparation and ARO grant W911NF-21-2-0147 for analysis. K. Watanabe and T.T. acknowledge support from the JSPS KAKENHI (grant no. 21H05233 and 23H02052), the CREST (JPMJCR24A5), JST and World Premier International Research Center Initiative (WPI), MEXT, Japan.

Author contributions H.Y. conceived the experiments. D.P., B.K., R.E., X.Z., K.D., M.G., S.H.P. and J.H.L. fabricated samples. D.P., B.K., R.E., H.-M.K., S.-G.K. and H.K. performed TEM experiments. D.P., C.P., E.K., B.K., H.-M.K., S.M.Y., K. Wang, P.K., Y.-W.S. and H.Y. analysed the data. C.P., E.K., K.Y. and Y.-W.S. performed theoretical analysis. K. Watanabet and T.T. grew bulk h-BN crystals. D.P., C.P., Y.-W.S. and H.Y. wrote the manuscript. All authors contributed to the overall scientific interpretation and edited the manuscript.

Competing interests The authors declare no competing interests.

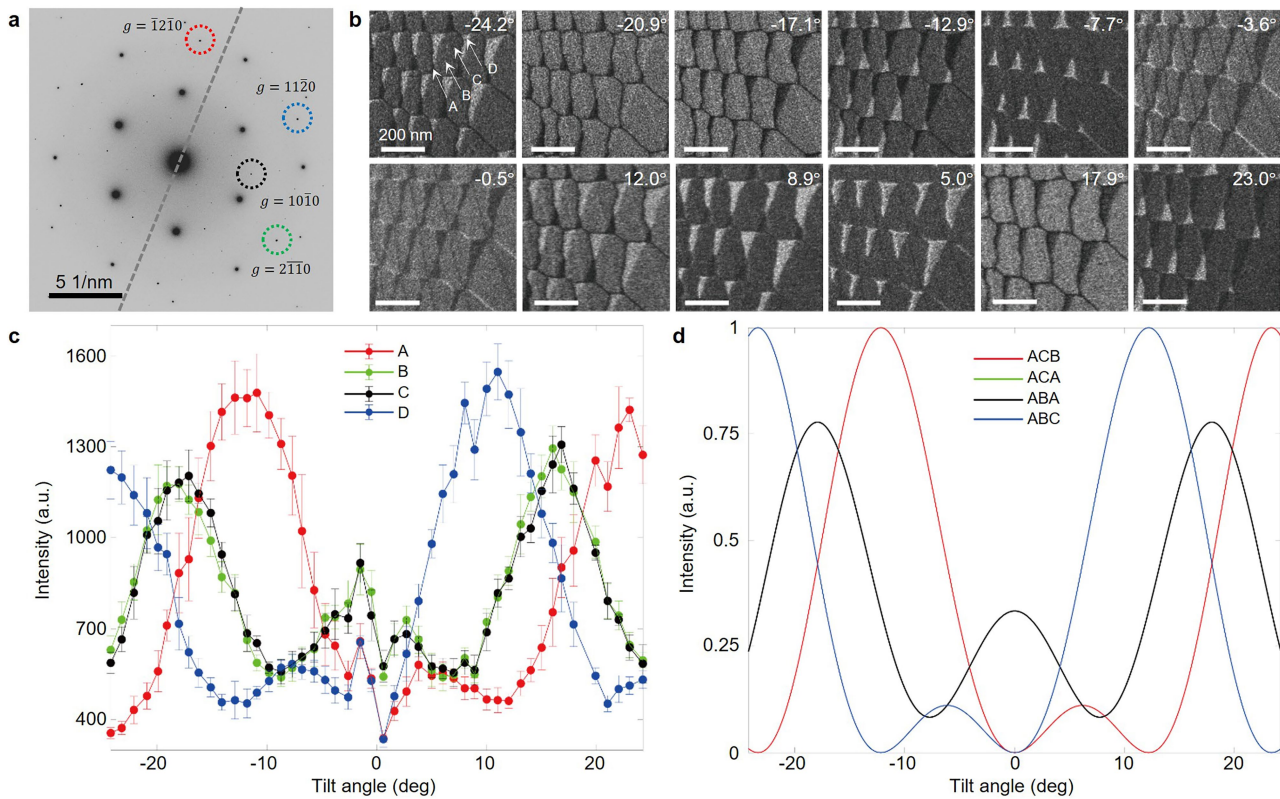
Additional information

Supplementary information The online version contains supplementary material available at <https://doi.org/10.1038/s41586-025-08932-0>.

Correspondence and requests for materials should be addressed to Young-Woo Son or Hyobin Yoo.

Peer review information *Nature* thanks Yung-Chang Lin, Junhao Lin and the other, anonymous, reviewer(s) for their contribution to the peer review of this work.

Reprints and permissions information is available at <http://www.nature.com/reprints>.



Extended Data Fig. 1 | Domain contrast image obtained by DF TEM analysis.

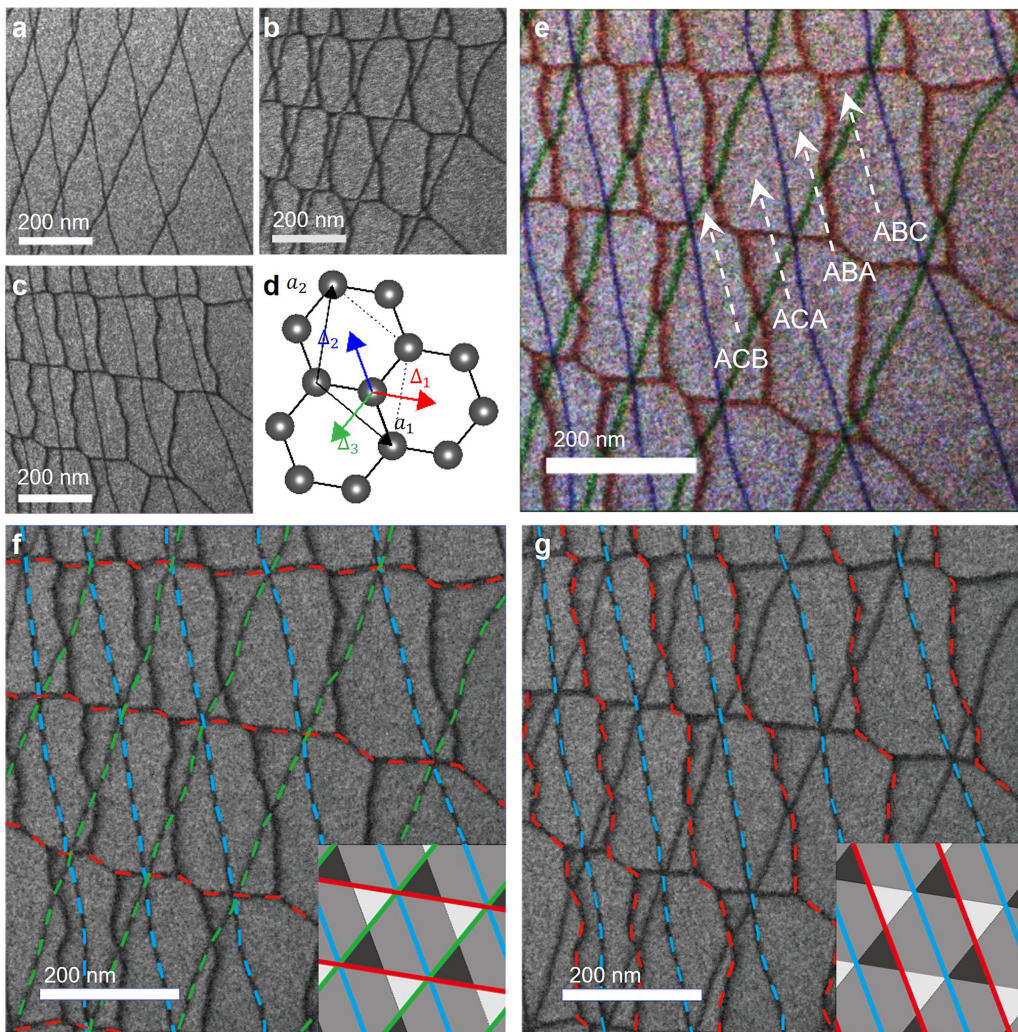
a. SAED pattern obtained from TTG. The first-order Bragg peak ($g=1\bar{0}\bar{1}0$) is marked with the black dashed circle and the three sets of second-order Bragg peaks, $g=\bar{1}\bar{2}\bar{1}0$, $g=11\bar{2}0$ and $g=2\bar{1}\bar{1}0$, are marked with red, blue and green dashed circles, respectively. A grey dashed line is drawn to denote the tilt axis.

b. A series of DF TEM images obtained as a function of specimen tilt angle in the electron microscope. Four distinct domains are marked as A, B, C and D.

c. Electron diffraction intensities experimentally measured from the four

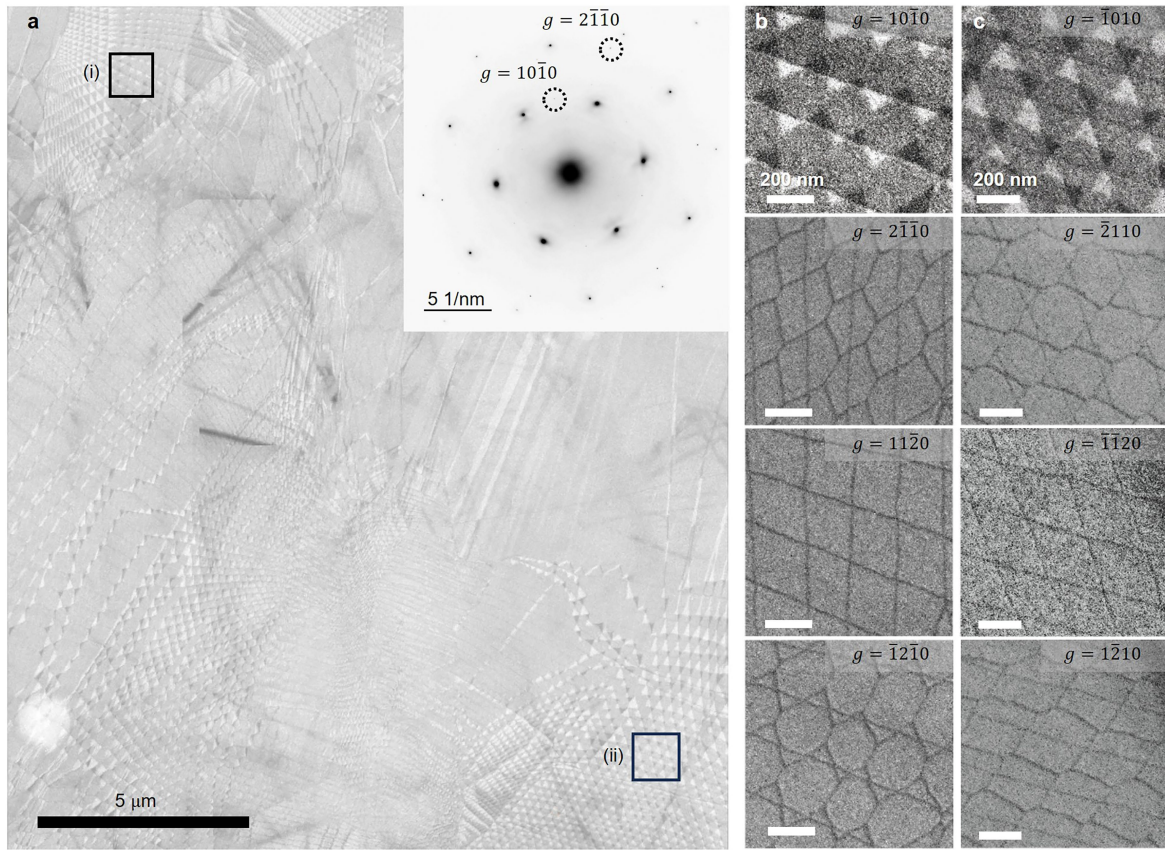
different domain regions as a function of tilt angle of the specimen. The red, green, black and blue curves correspond to the diffraction intensities obtained from the domains marked as A, B, C and D, respectively. The error bars represent the standard deviations of the intensities obtained from different domains with identical atomic configurations.

d. Simulated electron diffraction intensities obtained from different stacking orders in trilayer graphene. The red, green, black and blue curves correspond to the simulated diffraction intensity obtained from ACB, ACA, ABA and ABC stacking orders, respectively.



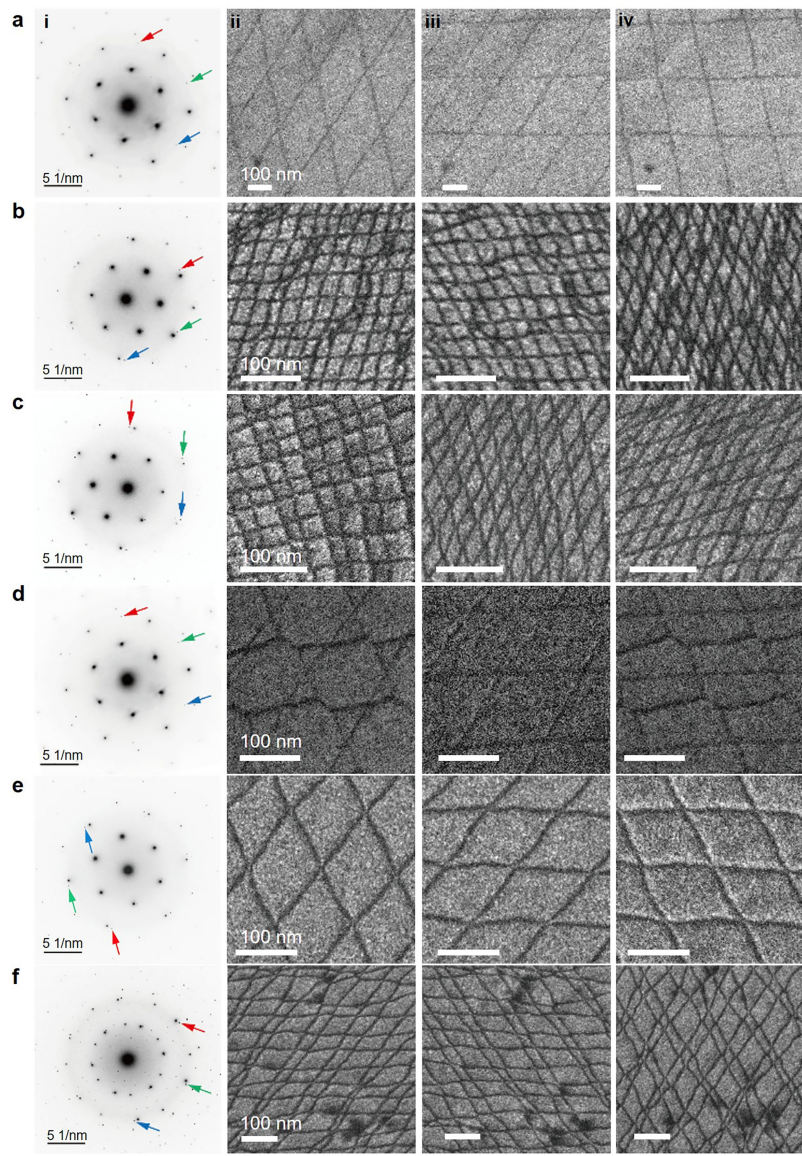
Extended Data Fig. 2 | DF TEM domain boundary contrast image obtained by DF TEM analysis. **a–c**, DF TEM images obtained from the second-order Bragg peaks. $g = \bar{1}2\bar{1}0$, $g = 1\bar{1}20$ and $g = 2\bar{1}\bar{1}0$ Bragg peaks are used to obtain the DF images shown in **a**, **b** and **c**, respectively. **d**, Schematic illustrating the displacement vectors Δ_i ($i = 1, 2, 3$) associated with the domain boundaries. The displacement vectors Δ_i are drawn on top of the atomic structure to denote the directions and magnitudes of the displacements. **e**, Composite-colour DF TEM image obtained from the three sets of DF images shown in Extended Data Fig. 2a–c by summing them after colour contrasting the individual images. As a result, the coloured lines indicate the domain walls with the characteristic displacement vectors shown in **d**. **f,g**, Distinct domain boundary networks formed at the adjacent interfaces. Domain boundary network formed at the bottom interface (**f**) and at the top interface (**g**) are drawn as coloured dashed lines. When the bottom interface is twisted with finite angle ($\theta_{23} \neq 0^\circ$),

a triangular domain-wall network appears as a result of the lattice reconstruction as in **f**. When the top interface exhibits the twist angle $\theta_{12} = 0^\circ$, a parallel array of domain walls appears. The insets in **f** and **g** represent the schematic drawings for kagome-like domain lattices, in which black and white regions represent the rhombohedral stacking orders and the grey regions indicate the Bernal stacking orders. The domain walls are visualized with distinct coloured lines, corresponding to the displacement vectors shown in **d** with the same colours. In the twisted interface (**f**), the directions of each domain wall are mostly parallel with the displacement vector, indicating that all of the domain walls can be characterized with the shear type of displacements. In the untwisted interface (**g**), one type of domain wall (marked by the red lines in **g**) exhibits the displacement vector that has a non-zero orthogonal component to the domain-wall direction, revealing that the uniaxial displacement is incorporated along such domain walls.



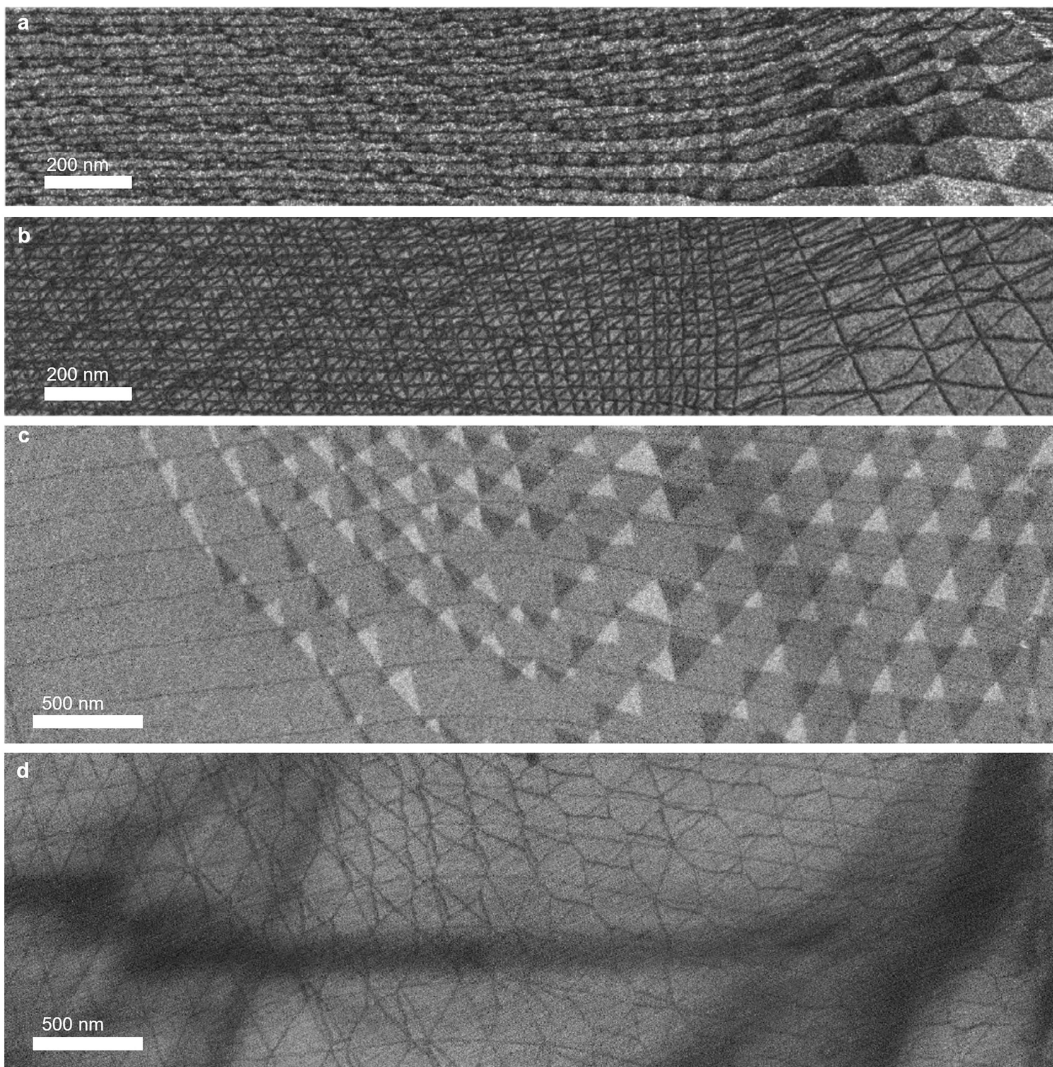
Extended Data Fig. 3 | SSB lattice reconstruction with distinct nematic orders. **a**, Low-magnification DF TEM image using the first-order Bragg peak to visualize the domain contrast. Inset shows the corresponding SAED pattern. **b**, $g = 10\bar{1}0$, $g = 2\bar{1}\bar{1}0$, $g = 1\bar{1}\bar{2}0$ and $g = \bar{1}2\bar{1}0$ DF TEM images obtained from the square region (i) in **a**. **c**, $g = \bar{1}010$, $g = \bar{2}110$, $g = \bar{1}\bar{1}20$ and $g = \bar{1}\bar{2}10$ DF TEM images

obtained from the square region (ii) in **a**. Figure 2h,i is obtained by summing the four different DF TEM images shown in **b** and **c**, respectively, to visualize the domain and domain-wall contrasts. Note that the nematic boundaries visualized in the $g = 2\bar{1}\bar{1}0$ DF TEM image in **b** and the $g = \bar{1}\bar{2}10$ DF TEM image in **c** adopt different directions, which are rotated 60° with respect to each other.



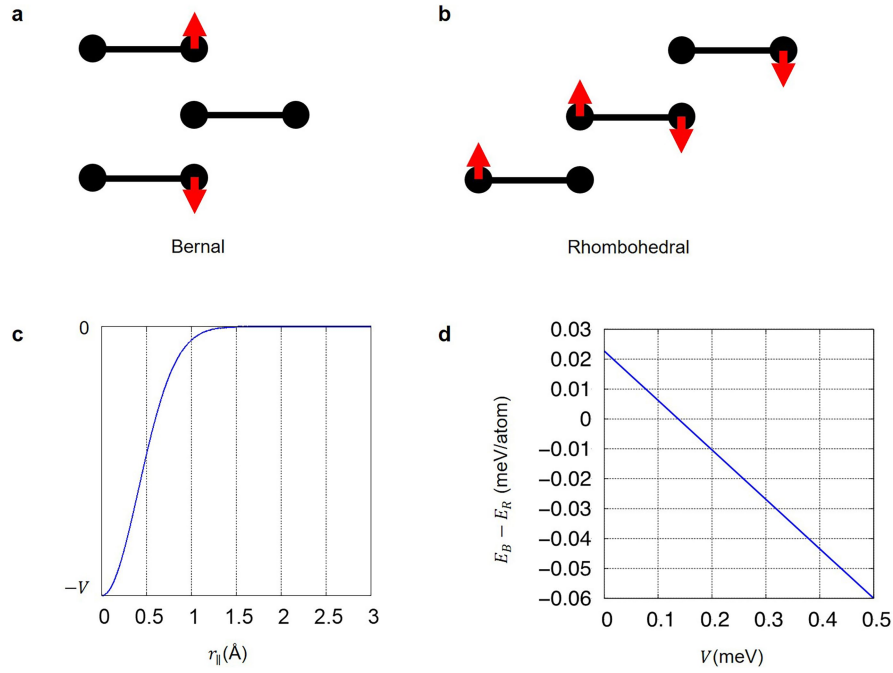
Extended Data Fig. 4 | Domain boundary contrast images obtained from TTG. **a–f**, SAED (panels (i)) and DF TEM images (panels (ii)–(iv)) using the three sets of second-order Bragg peaks obtained from TTG with various twist-angle combinations. Each of the Bragg peaks used to obtain DF TEM images shown in panels (ii)–(iv) are marked with red, green and blue arrows in the SAED images.

SAED and DF TEM images are obtained for the experimentally observed phases shown in the main text (Fig. 3): simple triangular domain lattice (**a**), simple triangular domain lattice bound by moiré-of-moiré boundaries (**b**), double-coloured triangular domain lattice (**c**), kagome-like domain lattice (**d**), coloured triangular domain lattice (**e**) and hexagonal domain lattice (**f**).



Extended Data Fig. 5 | Structural transition between different domain lattices. **a,b**, Domain contrast image ($g = 10\bar{1}0$ DF TEM image (a)) and the domain boundary contrast image (summation of $g = 2\bar{1}\bar{1}0$, $g = 1\bar{1}\bar{2}0$ and $g = \bar{1}2\bar{1}0$ DF TEM images (b)) obtained from the same region of the TTG specimen. Transition from the simple triangular domain lattice bound by moiré-of-moiré boundaries (left) to the double-coloured triangular domain lattice near the commensurate condition of $2\theta_{12} + \theta_{23} = 0$ (centre) to another locally

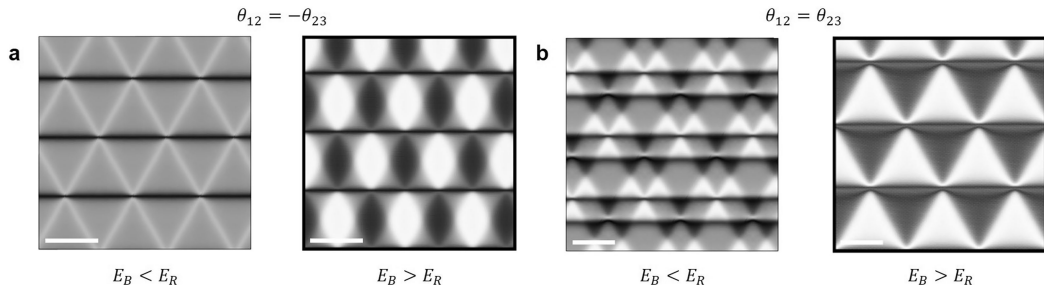
commensurate coloured triangular domain lattice (right). **c,d**, Domain contrast image ($g = 10\bar{1}0$ DF TEM image (c)) and the domain boundary contrast image (summation of $g = 2\bar{1}\bar{1}0$, $g = 1\bar{1}\bar{2}0$ and $g = \bar{1}2\bar{1}0$ DF TEM images (d)) obtained from another region of the TTG specimen. Transition from the simple triangular domain lattice (left) to the kagome-like domain lattice (right) is shown to exhibit complex local minimum domain configuration in the middle.



Extended Data Fig. 6 | Modified KC potential. Spurious out-of-plane displacement of Bernal-stacked (a) and rhombohedral-stacked (b) trilayer graphene. Red arrows indicate tiny but finite displacements around 1.4×10^{-3} Angstrom. c, Gaussian-type next-nearest-neighbour interlayer interaction potential that depends only on the plane-projected distance r_{\parallel} between carbon

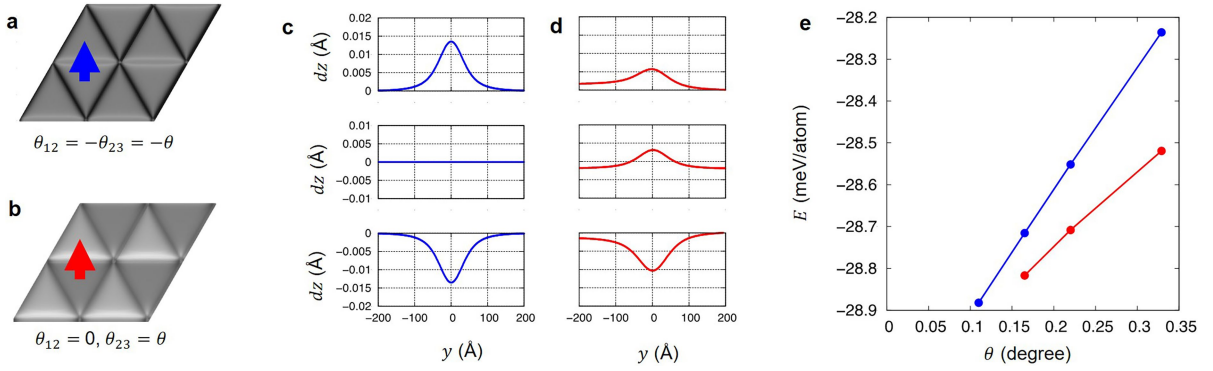
atoms on the top and bottom layers. d, The energy difference between Bernal (E_B) and rhombohedral (E_R) trilayer graphene as a function of control parameter V . Without V , E_B is larger than E_R with KC potential. With $V > 0.15$ meV, the Bernal stacking becomes more stable than the rhombohedral stacking.

Article



Extended Data Fig. 7 | Comparison of relaxed structures with different total energy configurations. **a**, Simulated TEM images for the alternate stacking case of $\theta_{12} + \theta_{23} = 0^\circ$, corresponding to panels (i) in Fig. 3. Grey colour corresponds to Bernal stacking and black and white colours to rhombohedral stacking. The left panel is a moiré domain pattern in the case of Bernal stacking

in the ground state and the right panel shows the fully relaxed domain pattern in the case that rhombohedral stacking has a lower total energy than Bernal stacking. **b**, Simulated TEM images for the helical stacking case of $\theta_{12} - \theta_{23} = 0^\circ$, corresponding to the panels (vi). The left and right panels are obtained with same conditions used in **a** and used same colour scheme. Scale bars, 100 nm.



Extended Data Fig. 8 | Structures and energies of the domain wall in TTG.
 Stacking domain structures of TTG for $\theta_{12} = -\theta_{23} = \theta$ (**a**) and $\theta_{12} = 0, \theta_{23} = \theta$ (**b**). The height variation dz along the blue (Bernal–Bernal boundary) and red (Bernal–rhombohedral boundary) arrows are drawn in **c** and **d**, respectively. In **c** and **d**, from the top to bottom are line profiles of dz for the top, middle and

bottom layers, respectively. **e**, Energies (E) of TTG as a function of θ for the cases in **a** and **b** are plotted with blue and red circles, respectively. From the slopes of $E(\theta)$, the energies of domain walls are estimated to be 137 and 84 meV Å⁻¹, respectively.